PHYSICAL REVIEW C **95**, 064913 (2017)

Hydrodynamic predictions for Pb+Pb collisions at 5.02 TeV

Scott McDonald,[1] Chun Shen,[1] François Fillion-Gourdeau,[2,3] Sangyong Jeon,[1] and Charles Gale[1]
[1]*Department of Physics, McGill University, 3600 University Street, Montreal, Québec H3A 2T8, Canada*
[2]*Université du Québec, INRS-Énergie, Matériaux et Télécommunications, Varennes, Québec J3X 1S2, Canada*
[3]*Institute for Quantum Computing, University of Waterloo, Waterloo, Ontario N2L 3G1, Canada*
(Received 5 December 2016; revised manuscript received 31 March 2017; published 28 June 2017)

Predictions and comparisons of hadronic flow observables for Pb+Pb collisions at 2.76 and 5.02 TeV are presented using a hydrodynamics + hadronic cascade hybrid approach. Initial conditions are generated via a new formulation of the IP-Glasma model and then evolved using relativistic viscous hydrodynamics and finally fed into transport cascade in the hadronic phase. The results of this work show excellent agreement with the recent charged hadron anisotropic flow measurements from the ALICE Collaboration of Pb+Pb collisions at 5.02 TeV. Event-by-event distributions of charged hadron v_n, flow event-plane correlations, and flow factorization breaking ratios are compared with existing measurements at 2.76 TeV, and are predicted at 5.02 TeV. Further predictions of identified hadron observables (for both light and multistrange hadrons), such as p_T-spectra and anisotropic flow coefficients, are presented.

DOI: 10.1103/PhysRevC.95.064913

I. INTRODUCTION

Relativistic heavy-ion collisions conducted at the Relativistic Heavy-Ion Collider (RHIC) and the Large Hadron Collider (LHC) create a deconfined state of quarks and gluons, known as quark-gluon plasma (QGP), at extreme temperatures and densities. Astonishingly, the strongly coupled nature of the QGP exhibits nearly perfect fluid behavior in experimental measurements. On the one hand, such collective phenomena are very hard to study from first principles due to the strong coupling that restricts our ability to use perturbative QCD techniques. On the other hand, the wealth of experimental data coupled with macroscopic phenomenological models can offer us reliable tools to quantitatively constrain the transport properties of the QCD matter. The measured momentum distributions of produced hadrons, namely particle transverse momentum spectra and the Fourier coefficients of their azimuthal distributions (known as anisotropic flow coefficients $\{v_n\}$), show stringent power to extract the transport properties of QGP [1,2]. In the spirit of precisely mapping out properties of QGP, hadronic observables in Pb+Pb collisions at $\sqrt{s} =$ 5.02 TeV center-of-mass energy were recently measured at the LHC [3].

In this work, we will confront this new data with a fully integrated state-of-the-art theoretical framework. For initial conditions, we rely on a new formulation of the IP-Glasma model, which provides realistic event-by-event fluctuations and nonzero preequilibrium flow at the early stage of heavy-ion collisions. Individual collision systems are evolved using relativistic hydrodynamics with nonzero shear and bulk viscosities [4]. As the density of the system drops, fluid cells are converted into hadrons and further propagated microscopically using a hadronic cascade model [5,6]. A quantitative description of various hadronic flow observables in Pb+Pb collisions 2.76 TeV is achieved within this framework. Regarding this as a base point, we extend our approach to study the dynamical evolution of Pb+Pb collisions at the higher 5.02 TeV. We will provide quantitative predictions for the flow observables of identified particles, namely particle spectra, mean p_T, and p_T-differential $v_{2,3,4}\{\mathrm{SP}\}(p_T)$, thus filling a void in the current literature of flow predictions in Pb+Pb collisions at 5.02 TeV [7–9]. The event-by-event distributions of charged hadron v_n are studied, for the first time, within such a hybrid approach at the two LHC collision energies. The flow event-plane correlations and flow factorization breaking ratios with IP-Glasma initial conditions are also investigated and compared with the existing ATLAS and CMS measurements at 2.76 TeV. Predictions of these correlation observables at 5.02 TeV are presented. All of these flow observables at the two LHC energies will help us to verify the validity of the hydrodynamic model framework and, more importantly, to set stronger constraints on the extraction of transport properties of the QGP, especially their temperature dependence.

The paper is organized as follows. Section II will provide an overview of the theoretical framework in three stages, beginning with a discussion on the new implementation of IP-Glasma and its underlying physics. Section II B will describe the centrality selection procedure that is employed for this work, and Sec. II C will briefly introduce the details of the hydrodynamic and hadronic cascade simulations. The latter section will focus on the details of the implementations and the parameters used as the physics of these models has been discussed in great detail elsewhere [4,10]. The procedure of our flow analysis is explained in Sec. II D. In Sec. III, we start the phenomenology discussion from inclusive charged hadron observables to identified particle flow coefficients. Their centrality and p_T-dependence results are compared to existing experimental measurements at 2.76 TeV. Predictions are made at the higher 5.02 TeV. Event-by-event flow distribution and event-plane correlations are studied in Sec. III C at the two LHC collision energies. Finally, conclusions will be outlined in Sec. IV. In the Appendix, effects from out-of-equilibrium correlations and hadronic scatterings in particle flow coefficients and their correlation functions are discussed.

 ©2017 American Physical Society

II. THEORETICAL FRAMEWORK

A. The IP-Glasma Model

Historically, the initial state of heavy ion collisions was dominated by geometric models such as the Monte Carlo Glauber model. In recent years, however, QCD based models that include saturation physics have come to define the standard in the field [11]. IP-Glasma, in particular, has proven itself to be an excellent model of the initial state.[1] First implemented in Refs. [13,14], IP-Glasma is based on the IP-Sat model presented in [15], and the glasma model [16–19]. It includes saturation physics as well as sub-nucleonic color charge fluctuations that give the model its trademark "spiky" initial conditions. This paper presents a new numerical implementation of IP-Glasma, the results of which will be presented in the next section. Numerical convergence of the energy density as a function of the lattice spacing was confirmed for relevant switching times, and the results were consistent with those of Ref. [20]. The simulations presented here utilize a lattice spacing of $dx = dy = 0.1$ GeV^{-1}, which is sufficient for convergence.

The IP-Glasma model begins by sampling nucleons from a Woods-Saxon distribution,

$$\rho(r)/\rho_0 = \frac{1}{1+\exp\left(\frac{r-R}{a}\right)} \tag{1}$$

where R is the nuclear radius and a is the nuclear skin depth. For ^{208}Pb, these parameters are set to $R = 6.62$ fm and $a = 0.546$ fm [21].[2] Once the spatial distribution of nucleons is sampled and projected onto the transverse plane, the saturation scale is determined through the IP-Sat framework [15]. The criterion for the saturation scale comes from requiring that the exponent of the Glauber-Mueller dipole cross section given by

$$\frac{d\sigma_{qq}}{d^2b} = 2\left[1-\exp\left(-\frac{\pi^2}{2N_c}r^2\alpha_s(\mu^2)xg(x,\mu^2)T(b)\right)\right] \tag{2}$$

equals 1/2, as

$$\left(\frac{\pi^2}{2N_c}r^2\alpha_s(\mu^2)xg(x,\mu^2)T(b)\right)\Big|_{r=r_s} = \frac{1}{2}. \tag{3}$$

This criterion equates to defining the saturation radius r_s as the dipole size for which the proton consists of one interaction length. Then the saturation scale is related to r_s via $Q_s^2 = 2/r_s^2$. The impact parameter dependence of the IP-Sat framework is introduced through the proton thickness function which is taken to be a Gaussian:

$$T_p(b) = \frac{1}{2\pi B_G}e^{\frac{-b_\perp^2}{2B_G}}, \tag{4}$$

where $B_G = 4.0$ GeV^{-2} is the average gluonic radius of the proton which follows from a fit to HERA diffractive data [24]. The gluon distribution function is initialized according to

$$xg\left(x,\mu_0^2\right) = A_g x^{-\lambda_g}(1-x)^{5.6} \tag{5}$$

with $\lambda_g = 0.058$ and $A_g = 2.308$ taken from Ref. [24], and $\mu_0^2 = 1.0$ GeV^2.[3] This distribution function is then evolved using the leading order Dokshitzer-Gribov-Lipatov-Altarelli-Parisi (DGLAP)[25–27] equations without quarks. The numerical solution to these equations appears in Ref. [28]. The scale relates to the dipole radius through

$$\mu^2 = \frac{4}{r^2} + \mu_0^2. \tag{6}$$

The average color charge is of course zero, but there are local fluctuations of color charge that give rise to a nonzero expectation value for the average squared color charge density. This quantity is proportional to the saturation scale squared $Q_s^2 \propto g^4\mu^2$. For the purposes of this paper, the constant of proportionality was determined by fitting the charged hadron multiplicity $dN_{ch}/d\eta$, a process which yielded $Q_s \approx 0.5g^2\mu$.[4] The color charge configuration is then sampled from a Gaussian with variance

$$\left\langle\rho^a_{A(B)}(\mathbf{x}_\perp)\rho^b_{A(B)}(\mathbf{y}_\perp)\right\rangle = g^2\mu^2_{A(B)}(x,\mathbf{x}_\perp)\delta^{ab}\delta^2(\mathbf{x}_\perp-\mathbf{y}_\perp), \tag{7}$$

where the subscripts A and B distinguish the two nuclei, where A moves in the $+z$ direction and B moves in the $-z$ direction. Once sampled, this color charge distribution comprises the eikonal color current that sources the small-x classical gluon fields in the color glass condensate framework,

$$J^\nu = \delta^{\nu\pm}\rho_{A(B)}(x^\mp,\mathbf{x}_\perp). \tag{8}$$

The gluon fields are then determined via the classical Yang-Mills (CYM) equations

$$[D_\mu, F^{\mu\nu}] = J^\nu. \tag{9}$$

Working in covariant gauge and light cone coordinates prior to the collision, the CYM equations boil down to the Poisson equation,

$$A^\pm_{A(B)} = -\frac{\rho_{A(B)}}{\nabla_\perp{}^2}. \tag{10}$$

The precollision fields are pure gauge and can be transformed to light-cone gauge, which is more physical after the collision, via the path-ordered Wilson Line,

$$V_{A(B)}(x_\perp) = P\exp\left(-ig\int dx^-\frac{\rho^{A(B)}(x^-,x_\perp)}{\nabla_\perp{}^2-m^2}\right) \tag{11}$$

which is discretized for the numerical simulation,

$$V_{A(B)}(x_\perp) = \prod_{i=1}^{N_y}\exp\left(-ig\frac{\rho_i^{A(B)}(x_\perp)}{\nabla_\perp^2-m^2}\right), \tag{12}$$

[1] The EKRT model is another such saturation based model. An overview of EKRT, as well as a brief comparison with the IP-Glasma model, can be found in Ref. [12].

[2] We checked that the initial eccentricities change by only a few percent if spatial configurations which includes nucleon-nucleon correlations [22] are used. Similar findings were shown in the MC-Glauber and the MCKLN models [23].

[3] In [13], $\mu_0^2 = 1.51$ GeV^2. This is the scale at which the gluon distribution is initialized, and it mostly effects the normalization of the energy density.

[4] $Q_s/(g^2\mu) \approx 0.75$ in [13].

where $N_y = 10$, and $m = \lambda_{QCD} = 0.2$ GeV is an infrared regulator that can be regarded as incorporating color confinement [29]. Then the pure gauge fields prior to the collision can be written as

$$A^i_{A(B)} = \theta(x^{-(+)})\frac{i}{g}V_{A(B)}(\mathbf{x}_\perp)\partial_i V^\dagger_{A(B)}(\mathbf{x}_\perp). \quad (13)$$

Due to our choice of lightcone gauge, the other components vanish:

$$A^{-(+)} = 0. \quad (14)$$

The gauge fields immediately after the collision can be found by matching the fields on the light cone [30,31],

$$A^i = A^i_A + A^i_B, \quad (15)$$

$$A^\eta = \frac{ig}{2}\left[A^i_A, A^i_B\right]. \quad (16)$$

The initial fields are then evolved using a lattice implementation of the sourceless CYM equations [32]. After evolving to a matching time of $\tau_0 = 0.4$ fm, the stress energy tensor is constructed from the chromo-electric and chromo-magnetic fields. For higher numerical accuracy in the lattice spacing, an improved expression has been used for the square of the longitudinal component of the chromo-magnetic field $(B^\eta)^2$ in the stress energy tensor, as compared to the expression used in Eq. (30) of [13]. This improves the numerical stability in solving the eigenvalue problem

$$T^\mu_\nu u^\nu = \varepsilon u^\mu, \quad (17)$$

which yields the local energy density ϵ and flow velocity u^μ that are used to initialize the hydrodynamic evolution.

In this work, the shear stress tensor $\pi^{\mu\nu}$ and bulk viscous pressure Π are set to zero at the initial time of our hydrodynamic simulations. We note that setting $\pi^{\mu\nu} = \Pi = 0$ introduces a discontinuity in matching the energy momentum current $T^{\tau\mu}$ from the Yang-Mills phase to the hydrodynamic phase at $\tau_0 = 0.4$ fm. An alternative way to avoid such a discontinuity is proposed in Ref. [33]. But this procedure modifies the spatial component of the $T^{\mu\nu}$ tensor at the matching. A more proper way to avoid this discontinuity is to initialize hydrodynamic simulations with the values of $\pi^{\mu\nu}$ and Π from the glasma phase. The RMS values of these dissipative components of the stress energy component $\sqrt{\pi^{\mu\nu}\pi_{\mu\nu}}$ and $|\Pi|$ are about 15% of the system's local enthalpy $\epsilon + P$ at $\tau_0 = 0.4$ fm. The effects of nonzero initial shear stress tensor on hadronic flow observables were studied in Ref. [34]. The influence on particle spectra and elliptic flow was shown to be negligible for the conditions used in that work. Thus, we defer a more quantitative study on the effects of initial $\pi^{\mu\nu}$ and initial bulk pressure Π with the IP-Glasma initial conditions to a future project.

B. Centrality selection

In relativistic heavy-ion experiments, the collision centrality of an event is determined by its measured charged hadron multiplicity. However, fully simulating the necessary number of minimum bias collisions is time-consuming. The system's initial total energy in the mid-rapidity region, $dE/d\eta_s|_{\eta_s=0}$, is proportional to the final charged hadron multiplicity, which serves as a good approximation in numerical simulations. The IP-Glasma model is made up of classical gluon fields that can interact at finite impact parameter, and such interactions contribute to the system's energy-momentum tensor. This subtlety leads to some ambiguity in determining the threshold for whether a collision occurred in the numerical simulation, a notion that corresponds to setting the 100% centrality boundary. In light of this, we sampled a large number of events in the impact parameter range $0 - 20$ fm, and sorted the events by their total energy at mid-rapidity, $dE/d\eta_s|_{\eta_s=0}$. We then simulated a subset (~200 events per 10% centrality bin) of the IP-Glasma initial conditions using our hybrid framework [4] to map the energy of IP-Glasma $dE/\tau d\eta_s|_{\tau=0.4}$, in units of GeV/fm, to the charged hadron multiplicity $dN_{\rm ch}/d\eta|_{|\eta|<0.5}$. We fit the results with a power law curve to determine the following empirical relationship:

$$\left.\frac{dN_{\rm ch}}{d\eta}\right|_{|\eta|<0.5} = 0.839\left(\left.\frac{dE}{\tau d\eta_s}\right|_{\tau=0.4\ \rm fm}\right)^{0.833}. \quad (18)$$

Using this formula, we varied the 100% centrality cutoff until the ratios of multiplicities between centrality bins, say $[dN_{ch}/d\eta(0\text{–}5\%)]/[dN_{ch}/d\eta(5\text{–}10\%)]$, matched the ratios from the experimental data. Once the 100% boundary was determined, all other centralities became fixed. We then adjusted the overall normalization by a factor of 0.89 to fix the magnitude of the energy density such that the measured $dN_{\rm ch}/d\eta|_{|\eta|<0.5}$ in 0–5% centrality was reproduced.

Our 100% centrality cutoff yields a geometric cross section that is consistent with measured values for the total cross section of Pb−Pb collisions at 2.76 TeV [35]. In terms of energy, at 5.02 TeV the 100% centrality cutoff corresponded to $dE/d\eta_s|_{\eta_s=0} \approx 11$ GeV. Taking the average particle transverse momentum to be 500 MeV, this amounts to the creation of ~22 particles per unit rapidity. This is comparable to high multiplicity $p + p$ events at the same energy [36], which are believed to constitute the lower bound for system size for hydrodynamics to be applicable. Thus our centrality cut is consistent with the hydrodynamics framework that we employ. To test the sensitivity of centrality selection on the choice of the cutoff energy, we varied the boundary by increasing the cutoff to $dE/d\eta_s|_{\eta_s=0} \approx 22$ GeV. We found that the charged hadron multiplicity in the central 0–5% centrality bin increased less than 1%. The centrality dependence of various hadronic observables was insensitive to the precise choice of this cutoff energy.

C. Hydrodynamics and hadronic cascade

We evolved 1500 IP-Glasma events per 10% centrality bin assuming boost-invariance in the longitudinal direction. Starting at $\tau_0 = 0.4$ fm, every IP-Glasma initial condition was matched to hydrodynamic variables, namely the local energy density and flow velocity via Eq. (17), and evolved using the state-of-the-art viscous hydrodynamic model MUSIC [37], together with the lattice QCD based equation of state (EoS), s95p-v1 [38]. Shear and bulk viscosities and their nonlinear coupling terms are included in the hydrodynamic evolution [39]. It has been shown using Bayesian methodology

that a nonzero temperature dependent bulk viscosity is favored by the data [11], and is necessary to describe transverse momentum and flow data simultaneously. In the hadronic phase, individual fluid cells are converted into particles on an isothermal hypersurface, $T_{\rm sw} = 145$ MeV, using the well-known Cooper-Frye procedure [40]. Each hydrodynamic freeze-out surface is oversampled for 100 events. Every sampled particle event is individually fed into the hadronic cascade model UrQMD [5,6] to simulate microscopically hadronic scatterings, baryon antibaryon annihilations, and resonance decays in the dilute hadronic phase. Particles are sampled in a boost-invariant fashion over 10 units of rapidity on the freeze-out surface. This ensures that the final particle sample after hadronic cascade remains boost invariant in the rapidity region -2.5 to 2.5. The leaking of particles at large forward and backward rapidities does not affect the mid-rapidity observables.

The switching temperature $T_{\rm sw}$ between the macroscopic hydrodynamic evolution and the microscopic transport description is fixed to reproduce the measured identified particle yields, especially the ratio between pion and proton yields [see Fig. 5(c) below]. Because the bulk viscosity at the freeze-out affects the particle yields, it can lead to a change in the switching temperature compared to the chemical freeze-out temperature from the thermal model fit [41]. In addition, the baryon and antibaryon annihilation in the hadronic transport phase changes the relative yields between mesons and baryons. It also affects the actual value of the switching temperature [42]. A detailed study on the hadronic observables dependence on the switching temperature is shown in Ref. [4,10]. The choices of specific shear and bulk viscosities have large effects on the development of hydrodynamic flow (both radial and anisotropic flow) during the evolution. We choose an effective $\eta/s = 0.095$ and a temperature dependent specific bulk viscosity $\zeta/s(T)$ in the simulations which provide a good description of charged hadron anisotropic flow coefficients and mean p_T measurements. The specific bulk viscosity is paramterized as follows:

$$\zeta/s(T) = 0.9 \times \begin{cases} 0.9e^{(\frac{T}{T_{\rm p}}-1)/0.0025} + 0.22e^{(\frac{T}{T_{\rm p}}-1)/0.022} + 0.03 & \text{for} \quad T < 0.95T_{\rm p}, \\ -13.77\left(\frac{T}{T_{\rm p}}\right)^2 + 27.55\left(\frac{T}{T_{\rm p}}\right) - 13.45 & \text{for} \quad 0.95T_{\rm p} < T < 1.05T_{\rm p}, \\ 0.025e^{-(\frac{T}{T_{\rm p}}-1)/0.025} + 0.25e^{-(\frac{T}{T_{\rm p}}-1)/0.13} + 0.001 & \text{for} \quad T > 1.05T_{\rm p}. \end{cases} \tag{19}$$

It is a parametrization based on Ref. [43,44]. The peak temperature of $\zeta/s(T)$ is set to $T_{\rm p} = 180$ MeV near the peak of the trace anomaly from the lattice calculation [45], where the conformal symmetry is maximally broken. In the current work, the same parametrization is used as in Ref. [4], except the overall normalization of $\zeta/s(T)$ is reduced by 10% to account for some small variations, $O(10\%)$, in the preequilibrium flow at $\tau_{sw} = 0.4$ fm.

After the hydrodynamic simulation, the spatial and momentum distribution of particles are sampled using the Cooper-Frye freeze-out procedure,

$$E\frac{dN}{d^3p}(x) = p^\mu d^3\sigma_\mu(x)[f_{\rm eq}(x,p) + \delta f(x,p)], \tag{20}$$

where $d^3\sigma_\mu(x)$ is the normal vector on the freeze-out hypersurface and $f_{\rm eq}(x,p)$ is particle's thermal equilibrium distribution function in a freeze-out fluid cell with local temperature $T(x)$. The out-of-equilibrium corrections $\delta f(x,p) = \delta f^{\rm shear}(x,p) + \delta f^{\rm bulk}(x,p)$ are the first-order shear and bulk viscous corrections to the thermal equilibrium distribution function. We used the same form of $\delta f^{\rm shear}$ and $\delta f^{\rm bulk}$ as in Ref. [4], assuming the relaxation time approximation:

$$\delta f^{\rm shear} = f_{\rm eq}(1 \pm f_{\rm eq})\frac{\pi^{\mu\nu}p_\mu p_\nu}{2T^2(e+P)} \tag{21}$$

and

$$\delta f^{\rm bulk} = f_{\rm eq}(1 \pm f_{\rm eq})\left(\frac{-\Pi}{\zeta/\tau_\Pi}\right)\frac{1}{3T}\left(\frac{m^2}{E} - \left(1 - 3c_s^2\right)E\right). \tag{22}$$

Here $\pi^{\mu\nu}$ is the shear stress tensor, Π is the bulk pressure, and τ_Π is the relaxation time for bulk viscosity. The effects of δf on hadronic flow observables will be discussed in the Appendix.

D. Flow analysis with finite number of particles

To compute hadronic flow observables, we first construct the flow vectors $\mathbf{Q}_n$ for each hydrodynamic event. The oversampled UrQMD events from the same hydrodynamic freeze-out surface are combined together into a superevent from which the $\mathbf{Q}_n$ vectors are computed,

$$\mathbf{Q}_n = \sum_{k=1}^{N_{\rm ev}^{\rm oversample}} \sum_{j=1}^{N_{\rm particle}^{k}} e^{in\phi_j}. \tag{23}$$

Here the index j runs over all particles in one UrQMD event with transverse momentum $p_T > 0.2$ GeV and the index k runs over all the UrQMD events initialized with particle samples from the same hydrodynamic hyper-surface. Since the oversample factor $N_{\rm ev}^{\rm oversample} = 100$ in our calculations, the large particle multiplicity reduces the random fluctuation in $\mathbf{Q}_n$ vector that arise from sampling a finite number of particles. The error of $\mathbf{Q}_n$ with respect to its value in the limit of an infinite number of particles can be estimated by calculating the event-plane resolution,

$$R_n = \sqrt{\left\langle \cos\left[n\left(\Psi_n^A - \Psi_n^B\right)\right]\right\rangle_{\rm hydro\,ev}} = \sqrt{\left\langle \frac{\mathbf{Q}_n^A \cdot \left(\mathbf{Q}_n^B\right)^*}{\left|Q_n^A\right|\left|Q_n^B\right|}\right\rangle_{\rm hydro\,ev}}. \tag{24}$$

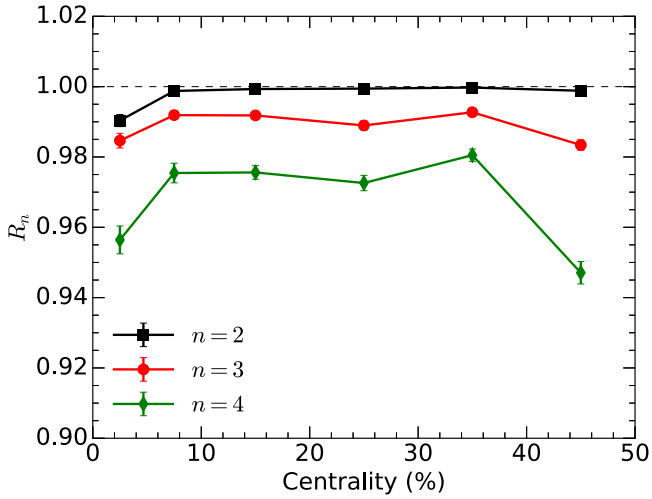

FIG. 1. The centrality dependence of the event plane resolution factor R_n for $n = 2,3,4$ in Pb+Pb collisions at 5.02 TeV.

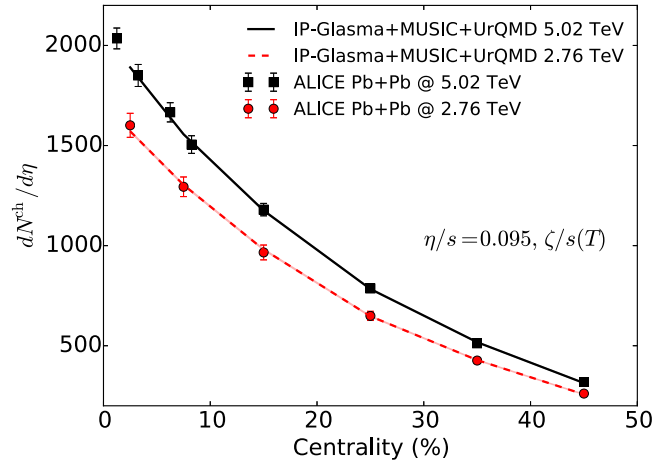

FIG. 2. The centrality dependence of charged hadron multiplicity in Pb+Pb collisions compared with the ALICE measurements at 2.76 TeV [48] and 5.02 TeV [49].

We choose the two subevents to be from the rapidity regions -2.5 to -0.5 and 0.5 to 2.5. The values of the event-plane resolution factors is shown in Fig. 1 as a function of centrality for $n = 2,3,4$. For elliptic flow, the deviation of R_2 from 1 is less than 1% from central to 50% centrality. The resolution gets slightly worse for higher order n. For v_4, the R_4 stays within 5% from unity. Compared to the typical values of R_n in the experiments [46], our resolution factor is much higher. Such a high resolution of the flow vector $\mathbf{Q}_n$ in every hydrodynamic event ensures that our theoretical event-by-event v_n distribution can be directly compared with the ATLAS measurements in which the finite resolution smearing was corrected using the Bayesian statistical unfolding method [47].

Because there is no correlation between particles from different UrQMD events, the short range nonflow correlation, such as correlations from resonance decays, is suppressed by the oversampling factor $N_{\rm ev}^{\rm oversample}$ when we compute the multiparticle correlation functions using the $\mathbf{Q}_n$ vectors. The two-particle cumulant flow coefficients are computed as

$$v_n\{2\} = \frac{\langle \mathrm{Re}\{\mathbf{Q}_n \cdot (\mathbf{Q}_n)^*\}\rangle_{\rm hydro\,ev}}{\langle N^2\rangle_{\rm hydro\,ev}}, \tag{25}$$

and the p_T-differential flow coefficients from the scalar product method is

$$v_n\{\mathrm{SP}\}(p_T) = \frac{\left\langle \mathrm{Re}\left\{\mathbf{Q}_n(p_T)\cdot\left(\mathbf{Q}_n^{\rm ref}\right)^*\right\}\right\rangle_{\rm hydro\,ev}}{\langle N(p_T)N^{\rm ref}\rangle_{\rm hydro\,ev} v_n\{2\}}. \tag{26}$$

Here $\mathrm{Re}\{\cdots\}$ takes the real part of the correlation function and $N^{\rm ref}$ and $N(p_T)$ are the corresponding particle multiplicities for $\mathbf{Q}_n^{\rm ref}$ and $\mathbf{Q}(p_T)$ vectors, respectively.

III. RESULTS AND DISCUSSION

In this section, we will start by comparing the numerical model to existing experimental measurements of Pb+Pb collisions at 2.76 TeV. By regarding the good descriptions of the existing experimental data as a base point, we extrapolate our calculation to higher collision energy and make predictions and postdiction for various hadronic flow observables.

A. Charged hadron yields and anisotropic flow

To calibrate our hybrid simulations to the desired collision energies, we adjust an overall normalization factor on the system's energy density such that the final charged hadron multiplicity agrees with the experimental measurements. In Fig. 2, charged hadron multiplicities at mid-rapidity are shown as a function of collision centrality for Pb+Pb collisions at 2.76 and 5.02 TeV. We used the same overall normalization $\sim$0.89 on the initial energy density to reproduce the measured $dN^{\rm ch}/d\eta|_{|\eta|<0.5}$ in 0–5% most central collisions at both collision energies. The centrality dependence of the charged hadron multiplicity is well described by the IP-Glasma model. The viscous entropy production during the hydrodynamic evolution is found to be about $O(10\%)$ compared to the initial entropy in the system.

Charged hadron anisotropic flow coefficients are shown as a function of collision centrality in Fig. 3. With $\eta/s = 0.095$ and $\zeta/s(T)$ in Eq. (19), our hybrid simulations can reproduce ALICE measurements for $v_2\{2\}$, $v_3\{2\}$, and $v_4\{2\}$ up to 40–50% semiperipheral collisions at 2.76 TeV quite well, as shown in Fig. 3(a). The simultaneous description to all the v_n coefficients as well as to their event-by-event distribution (see Fig. 11 below) suggests that our new formulation of the IP-Glasma model is consistent with previous works [4,13,14]. Now, by keeping the same values for the transport coefficients in hydrodynamic simulations, our $v_n\{2\}$ results in Pb+Pb collisions at 5.02 TeV agree with the latest ALICE data within small experimental error bars [3]. In our simulations, the charged hadron $v_2\{2\}$ increased by $(4.1 \pm 1.7)\%$, $v_3\{2\}$ by $(5.1 \pm 2.2)\%$, and $v_4\{2\}$ by $(6.2 \pm 2.3)\%$ from 2.76 to 5.02 TeV. The relative increase of $v_n\{2\}$ agrees with the experimental values reported in Ref. [3]. The initial eccentricities ε_n do not change at the two collision energies in the IP-Glasma model. The increase of v_n is due to the longer fireball lifetime at the higher collision energy, which converts more initial

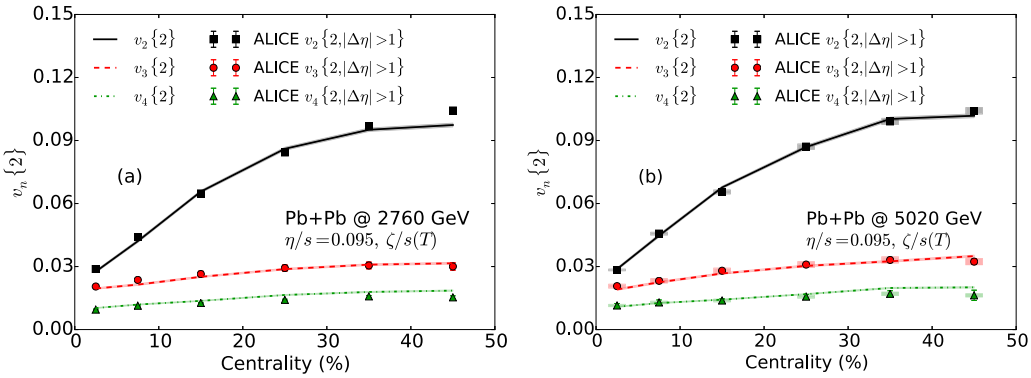

FIG. 3. The centrality dependence of charged hadron anisotropic flow coefficients in Pb+Pb collisions at 2.76 TeV (a) and 5.02 TeV (b). The integrated p_T range for the two particle cumulant $v_n\{2\}$ is from 0.2 to 3.0 GeV. Theoretical results are compared with the recent ALICE measurements at both collision energies [3,50].

spatial eccentricity into final particle momentum anisotropy. The fact that the same effective $\eta/s = 0.095$ can quantitatively reproduce the p_T-integrated charged hadrons v_n at the two collision energies suggests the temperature ranges probed by the fireball are quite similar. At the initial time $\tau_0 = 0.4$ fm, the peak temperature of the system can reach to ∼450 MeV in central Pb+Pb collisions at 2.76 TeV. The ∼80% increase in the collision energy results in a peak temperature that is about 20 MeV higher at 5.02 TeV.

In Fig. 4, charged hadron p_T-differential $v_n(p_T)$ are computed using the scalar-product method [51] and compared with the ALICE measurements at the two collision energies [3,50]. In the top 0–5% centrality, our hybrid approach describes the ALICE data within 10% up to 2 GeV for all the v_n coefficients. The agreement becomes limited to lower p_T in 30–40% peripheral collisions. Charged hadron v_n at high p_T are overestimated by 30% at $p_T = 2$ GeV. However, we should note that particles' p_T spectra are underestimated for $p_T > 1.5$ GeV in 30–40% centrality (see Fig. 6 below). In this intermediate p_T region, one would expect that the contribution from jet shower and minijets begins to play an important role. The inclusion of these components will affect the charged hadron $v_n(p_T)$ in this intermediate p_T range [52–55]. The quality of the model for data descriptions is similar at the two collision energies. Compared to the Ref. [56], the agreement with the measured $v_n(p_T)$ is worse. This difference is due to the inclusion of bulk viscosity. The bulk viscosity plays a critical role in reducing the hydrodynamic radial flow and improves the description of the experimental measured mean p_T [4]. At the same time, the inclusion of bulk viscosity requires a reduction

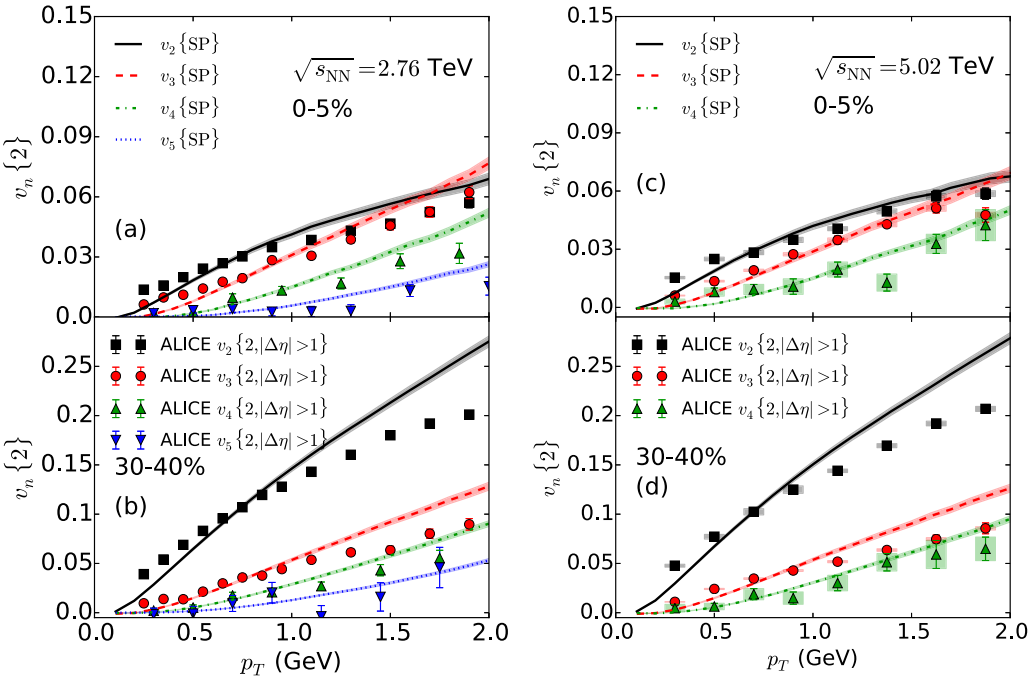

FIG. 4. Charged hadron p_T-differential v_n in 0–5% (a,c) and 30–40% (b,d) centrality bins in Pb+Pb collisions at 2.76 (a,b) and 5.02 (c,d) TeV. The reference flow vector is the charged hadron v_n integrated from 0.2 to 3.0 GeV. At both collision energies, theoretical results are compared with the ALICE measurements [3,50].

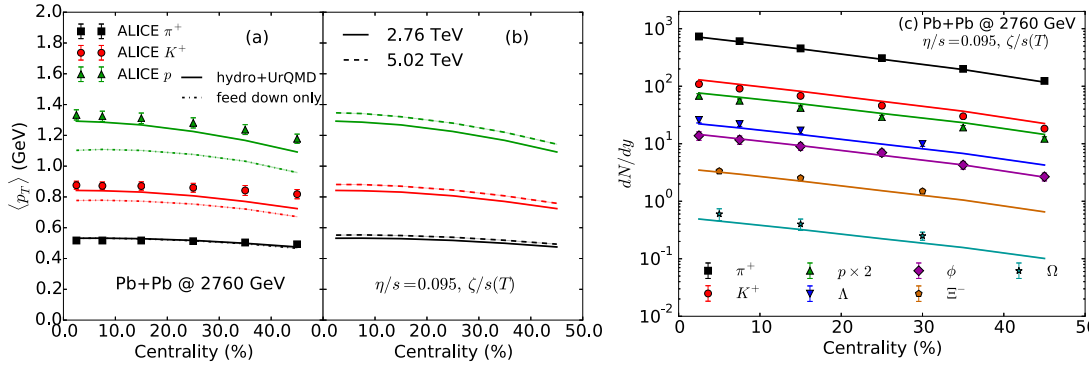

FIG. 5. (a) Identified particle averaged momentum, $\langle p_T \rangle$, as functions of centrality in Pb+Pb collisions at 2.76 TeV compared with the ALICE data [57]. (b) Predictions of π^+, K^+, and p mean p_T in Pb+Pb collisions at 5.02 TeV. (c) Identified particle yields as functions of centrality compared to the ALICE data.

in shear viscosity in order to describe the integrated v_n. Including the bulk viscosity and reducing the shear viscosity alter the shape of the p_T dependence of the differential flow harmonics. The effect of out-of-equilibrium correction δf on p_T-differential v_n is investigated in the Appendix.

B. Identified particle observables

While charged hadron v_n reflects a detailed flow pattern of the evolving medium at final kinetic freeze-out, identified particle observables, especially heavy baryons, are more sensitive to the background hydrodynamic flow. Furthermore, because the multistrange hadrons, such as ϕ, Λ, Ξ^-, and Ω, have small scattering cross sections in the hadronic phase, their observables can shed light on how the medium flows at an earlier time prior to the kinetic freeze-out of the other light hadrons.

Hydrodynamic radial flow blueshifts individual hadrons to higher p_T, which increases their average transverse momentum. In Fig. 5(a), we compare light hadron mean p_T's as a function of centrality with the ALICE measurements [57]. The $\langle p_T \rangle$ of π^+ agrees with experimental measurements through all centralities, while the proton mean p_T in the semiperipheral centralities are underestimated by $\sim$10%. The dash-dotted lines represent results in which hadronic rescatterings were turned off. Although the light π^+ mean p_T is barely affected, hadronic scatterings increase the proton $\langle p_T \rangle$ by 30%. This reflects that heavier protons show a larger sensitivity of hydrodynamic radial flow compared to the lightest π. In Fig. 5(b), we provide predictions for π^+, K^+, and proton mean p_T at 5.02 TeV. Compared to the results at 2.76 TeV, the mean p_T of π^+, K^+, and p increase by 4–5%. In Fig. 5(c), we compared the identified particle yields with the ALICE measurements in Pb+Pb collisions at 2.76 TeV. Our calculation agrees with the experimental data within the statistical errors. The centrality dependence is reproduced. We noted that the yields of strange hadrons ϕ, Ξ, and Ω are well described. Understanding the production of strange hadrons is an important topic for lattice QCD calculations [58,59].

Figures 6(a) and 6(c) present comparisons of π^+, K^+, and proton spectra with the ALICE data [57] in 0–5% and 30–40% centralities Pb+Pb collisions at 2.76 TeV. Consistent with the mean p_T results shown in Fig. 5(a), our hybrid model can reproduce the π^+ spectra up to 2 GeV in 0–5% centrality. The deviation from the data starts at $p_T \sim 1.5$ GeV, in the 30–40% centrality bin. Again, the contribution from jet showers and minijets is expected to be important in this intermediate p_T range [55]. The agreement with the heavier proton spectra extends to higher p_T. This is mainly because heavier protons receive a stronger blueshift effect from the hydrodynamic radial flow. The predictions of identified particle spectra are presented in Figs. 6(b) and 6(d). Besides the increase in particle yields, the identified particle spectra are flatter, reflecting a stronger radial flow developed at the higher collision energy.

The spectra of multistrange particles are shown in Fig. 7. Since ϕ mesons are unstable, we need to reconstruct them from

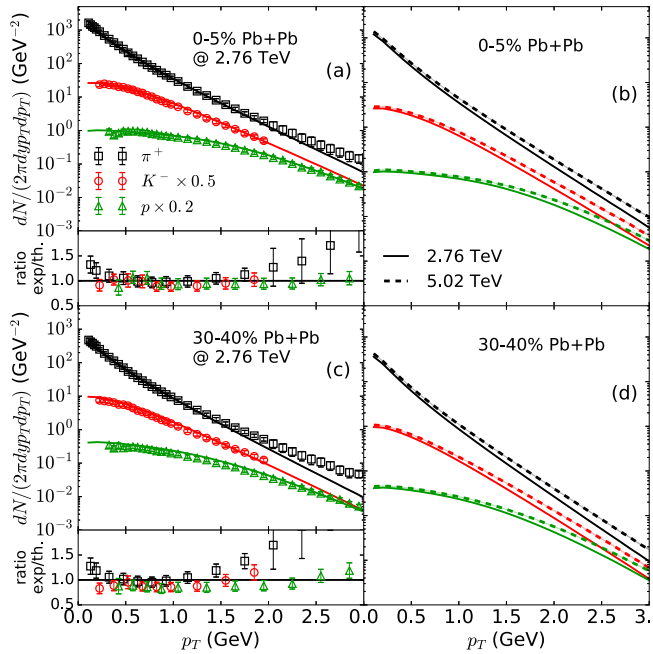

FIG. 6. (a,c) Light hadrons p_T-differential spectra in 0–5% and 30–40% Pb+Pb collisions at 2.76 TeV compared with the ALICE measurements [57]. (b,d) Predictions of π^+, K^+, and p spectra in Pb+Pb collisions at 5.02 TeV.

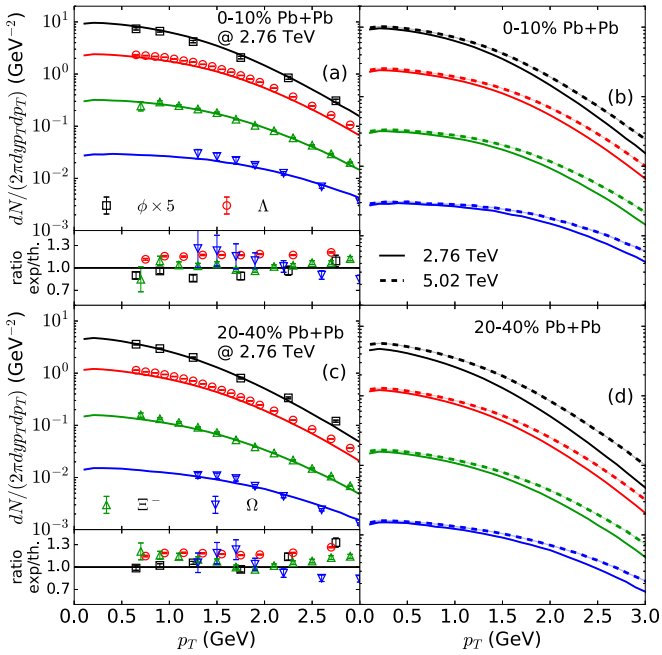

FIG. 7. (a,c) Multistrange hadrons p_T-differential spectra in 0–10% and 20–40% Pb+Pb collisions at 2.76 TeV compared with the ALICE measurements [60–62]. (b,d) Predictions of ϕ, Λ, Ξ^-, and Ω spectra in Pb+Pb collisions at 5.02 TeV.

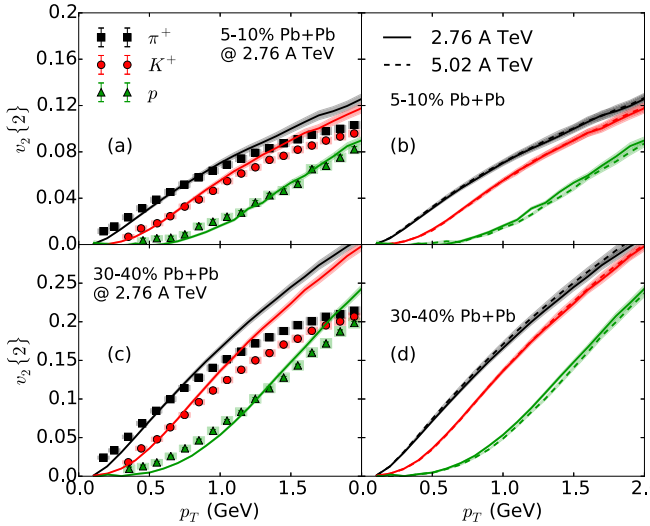

FIG. 8. (a,c) The elliptic flow coefficients v_2 of identified particles in 5–10% and 30–40% Pb+Pb collisions at 2.76 TeV compared with the ALICE measurements [64]. The reference flow vector is the charged hadron v_2 integrated from 0.2 to 3.0 GeV. (b,d) Predictions of the $v_2(p_T)$ for π^+, K^+, and p in Pb+Pb collisions at 5.02 TeV.

their decay daughters. We use K^+K^- pairs to reconstruct ϕ mesons as described in the experimental analysis of Ref. [62]. In the UrQMD results, in addition to checking that the invariant mass of K^+K^- pairs is at the ϕ resonance peak, $M = 1.019 \pm 0.00433$ GeV [63], we require the last interactions of both K^+ and K^- to be from decay processes and to be from the same space-time positions. Using these criteria, we can avoid the sophisticated statistical background subtraction performed in the experimental analysis [62]. Finally, we correct the absolute yield of the ϕ meson by its decay branching ratio to K^+K^- pairs, $B_r(\phi \to K^+K^-) = 0.489$ [63]. Please note that in our reconstruction method, if a daughter kaon from a decay scatters with other particles in the hadronic phase, its mother ϕ meson will not be reconstructed, as in the experimental reconstruction procedure. Thus, the yield of reconstructed ϕ can be directly compared to the measurements in Ref. [62]. Figures 7(a) and 7(c) show that our reconstructed ϕ meson samples provide an excellent description of the ALICE measured spectra up to 3 GeV [62]. Both the absolute yield and the shape of ϕ meson spectra are well reproduced.

In the strange baryon sector, the Λ measurement from ALICE [61] receives feed-down contributions from Σ^0 baryons. This weak decay channel $\Sigma^0 \to \Lambda + \gamma$ is not included in the UrQMD simulations. Thus, we perform two-body decays of Σ^0 to Λ as an afterburner in our simulations after the system is kinetically frozen out. Since the lifetime of Σ^0 is about 2000 fm/c, such decay processes will happen outside the fireball. This feed down contribution is about 30% compared to the thermally produced Λ yield. Figures 7(a) and 7(c) shows our spectra of Λ, Ξ^-, and Ω compared with the ALICE measurements. We underestimated the measured Λ spectra by $\sim$15% in both central and semiperipheral centrality bins. The shapes of spectra are well reproduced. The spectra of multistrange baryons Ξ^- and Ω show good agreements with the ALICE data [60]. Predictions of strange hadrons spectra in Pb+Pb collisions at 5.02 TeV are presented in Figs. 7(b) and 7(d). Similar to the light hadron spectra, the stronger hydrodynamic radial flow at higher collision energy produces flatter spectra for multistrange particles.

The p_T-differential v_n of identified hadrons can tell us how the momentum anisotropy of the system is distributed over different species of particles as a function of their transverse momentum. Figures 8(a) and 8(c) show comparisons for identified hadron $v_2(p_T)$ between our hybrid approach and the ALICE measurements at 2.76 TeV. The trend of agreement for pion $v_2^{\pi^+}(p_T)$ is similar compared to the situation for the charged hadron $v_2(p_T)$ shown in Fig. 4. The agreement with data extends to higher p_T for heavier protons. This is mainly because the stronger blueshift from radial flow improves the model description of the proton spectra as shown in Fig. 6, which helps the system to distribute the proton's momentum anisotropy properly into different p_T bins. Predictions at 5.02 TeV are presented in Figs. 8(b) and 8(d). Compared to the $v_2(p_T)$ at 2.76 TeV, the variation at higher collision energy is very small. This is a consequence of the canceling effects between the increase of p_T-integrated v_2 and stronger radial flow [65]. The former increases the differential v_2 at a fixed p_T while the latter blueshifts the particles carrying large momentum anisotropy to the higher p_T region. The $v_2(p_T)$ of light hadrons remains unchanged. For proton $v_2(p_T)$, one can see that the blueshift effect slightly wins over the increase of elliptic flow. The proton $v_2(p_T)$ at higher collision energy is blueshifted to higher p_T [66]. Higher order harmonic flow coefficients, v_3 and v_4, of identified particles are shown in Fig. 9. Comparisons with the ALICE measurements [67] show

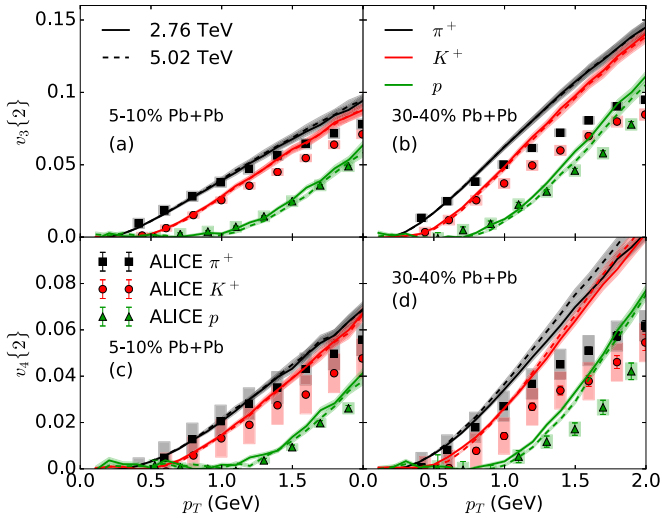

FIG. 9. Higher order anisotropic flow coefficients, $v_{3,4}\{2\}(p_T)$, for π^+, K^+, and p in Pb+Pb collisions at 2.76 and 5.02 TeV. The reference flow vector is the charged hadron v_n integrated from 0.2 to 3.0 GeV. The ALICE measurements at 2.76 TeV [67] are shown for comparison.

quality similar to the v_2 comparison in Fig. 8. Compared to elliptic flow, the mass splittings between π^+ and proton are larger for higher orders of n [68]. Predictions at 5.02 TeV are presented as dashed curves. The collision energy dependence of identified particle $v_{3,4}(p_T)$ is similar to those of elliptic flow.

Figure 10 shows the elliptic flow coefficients of ϕ, $\Lambda + \bar{\Lambda}$, and $\Xi^- + \bar{\Xi}^+$ from our hybrid calculations. Compared with the ALICE measurements at 2.76 TeV, the multistrange hadron

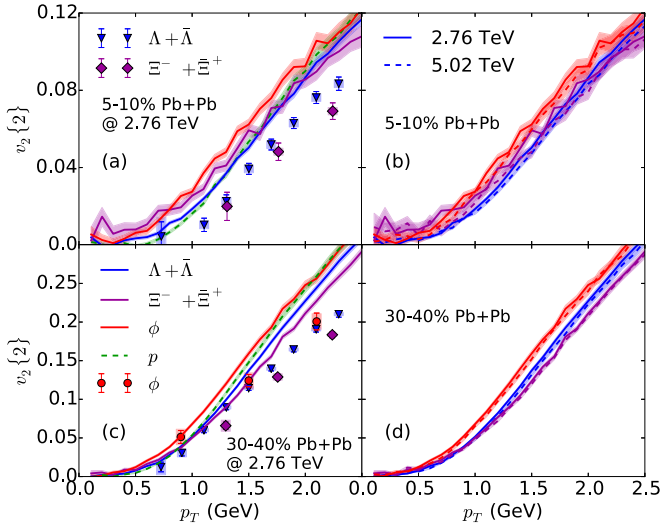

FIG. 10. (a,c) The elliptic flow coefficients v_2 of multistrange hadrons ϕ, $\Lambda + \bar{\Lambda}$, and $\Xi^- + \bar{\Xi}^+$ in 5–10% and 30–40% Pb+Pb collisions at 2.76 TeV compared with the ALICE measurements [64]. The reference flow vector is the charged hadron v_2 integrated from 0.2 to 3.0 GeV. (b,d) Predictions of the $v_2(p_T)$ for ϕ, $\Lambda + \bar{\Lambda}$, and $\Xi^- + \bar{\Xi}^+$ in Pb+Pb collisions at 5.02 TeV.

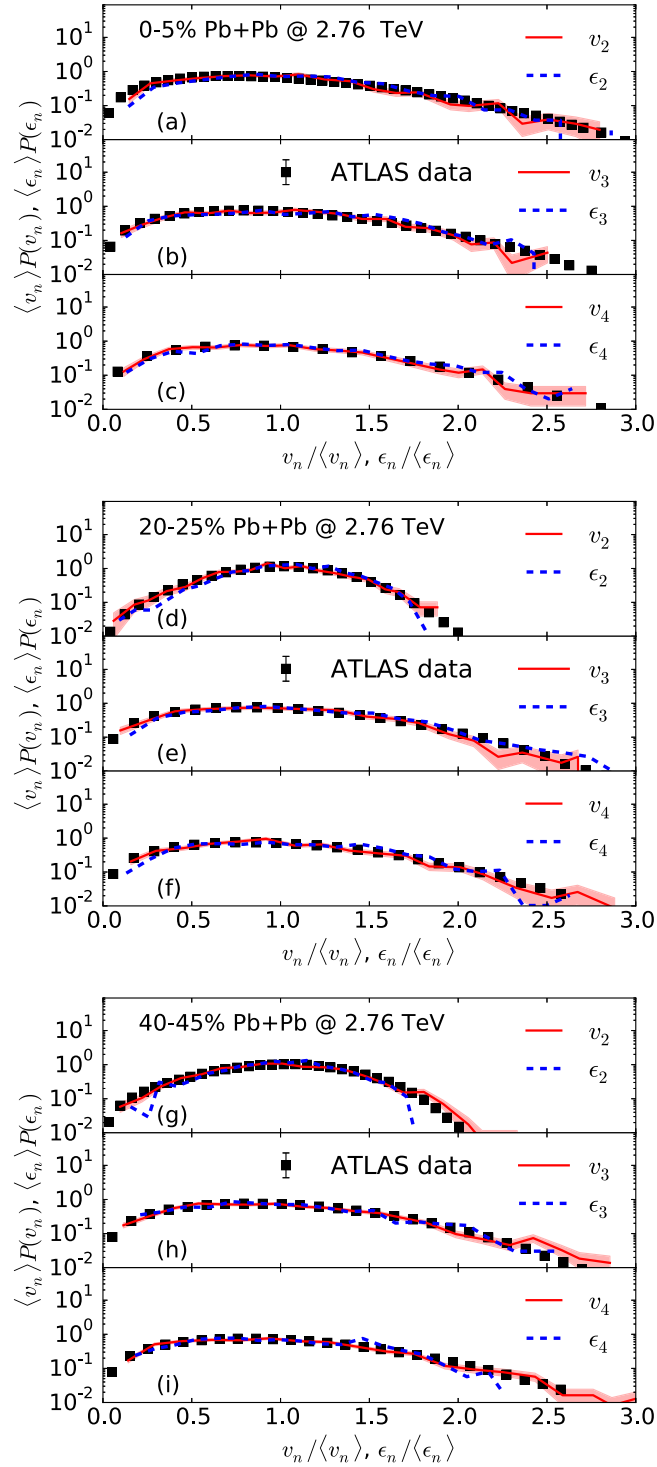

FIG. 11. The normalized distributions of event-by-event charged hadron anisotropic flow coefficients are compared with the measurements from the ATLAS Collaboration in 0–5% (a–c), 20–25% (d–f), and 40–45% (g–i) centralities in Pb+Pb collisions at 2.76 TeV [47]. The charged hadron v_n in every event are integrated from 0.5 to 3.0 GeV in transverse momentum. The normalized distributions of initial eccentricities at the end of the IP-Glasma phase ($\tau_0 = 0.4$ fm) are shown as dashed lines.

$v_2(p_T)$ are less blueshifted. Because of the small scattering cross sections in the hadron transport phase, these multistrange hadrons do not pick up enough blueshift from the "pion wind." The mass ordering of $v_2(p_T)$ of multistrange hadrons is violated compared to proton $v_2(p_T)$. A similar trend was found in other hybrid calculations [69–72]. The same problem exists at both collision energies.

C. Flow distribution and correlations

With model parameters being fixed by hadronic spectra and flow measurements, the following correlation observables are "parameter-free" predictions from our framework. These observables can further test the fluctuation spectrum of the initial state as well as the hydrodynamic response from which flow correlations are generated.

In Ref. [56], the authors first showed that IP-Glasma initial conditions coupled to viscous hydrodynamic simulations can reproduce the measured event-by-event distribution of charge hadron v_n quite well [47]. In Figs. 11, we show that the same quality of agreement can be achieved with a fully integrated hybrid approach which includes both shear and bulk viscosities. By comparing to the normalized distributions of initial eccentricities at the beginning of the hydrodynamic evolution, we find that the shapes of the v_n distributions in central to semiperipheral centrality bins are largely determined by initial state fluctuations. Hence, in these collisions the normalized v_n distributions reflect the nature of initial state fluctuations in heavy-ion collisions. In the more peripheral 40–45% centrality, the sequential hydrodynamic evolution and the hadronic transport dynamics modify the tails of the v_2 and v_4 distributions. This is understood as linear and cubic response in anisotropic flow harmonics [12,73]. Predictions of the event-by-event charged hadron v_n distributions in Pb+Pb collisions at 5.02 TeV are shown in Figs. 12. The shapes of the normalized v_n distributions are very close to those at 2.76 TeV. With about twice of the collision energy, the changes in the saturation scale in the IP-Glasma model are not large enough to affect the event-by-event distribution of the initial eccentricities, which imprint themselves on the final charged hadron v_n distributions. This is consistent with the recent ALICE flow cumulant measurement in Ref. [3], which showed that the relative increase in $v_2\{2\}$ and $v_2\{4\}$ are the same within statistical error bars. This means that the normalized variance of the v_2 distribution, which can be estimated as $\sigma^2_{v_2}/\langle v_2\rangle^2 = (v_2^2\{2\} - v_2^2\{4\})/(v_2^2\{2\} + v_2^2\{4\})$, remains unchanged when the collision energy increases by 80%.

Event-by-event fluctuations in heavy-ion collisions also result in nontrivial correlations among different orders of harmonic flow coefficients. In Fig. 13, we compute the two and three event-plane correlations from our hybrid simulations and compare them with the ATLAS measurements in Pb+Pb collisions at 2.76 TeV [74]. We used the scalar-product method to compute these correlators [75],

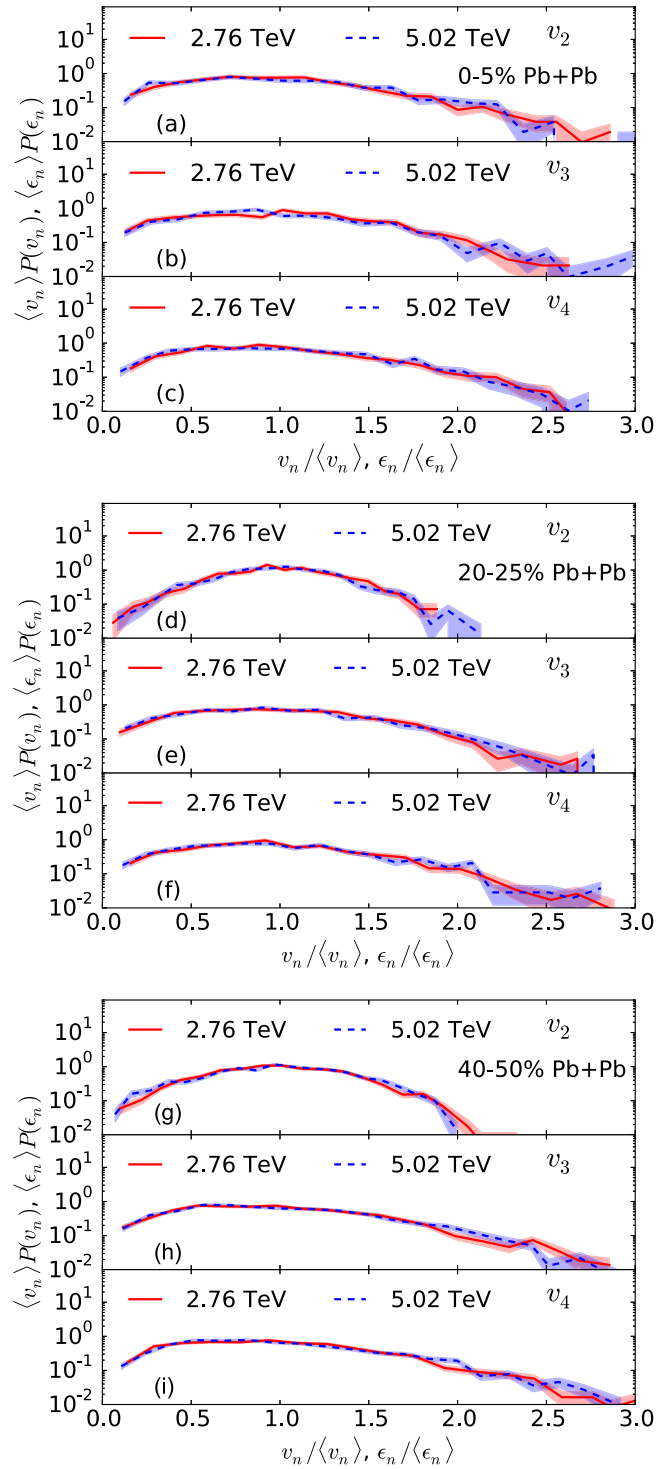

FIG. 12. Predictions of event-by-event charged hadron v_n distributions in 0–5%, 20–25%, and 40–50% Pb+Pb collisions at 5.02 TeV.

$$\cos\left[c_1 n_1 \Psi_{n_1} - c_2 n_2 \Psi_{n_2}\right] = \frac{\mathrm{Re}\left\{\langle \mathbf{Q}_{n_1}^{c_1} (\mathbf{Q}_{n_2}^{c_2})^*\rangle\right\}}{\sqrt{\langle \mathbf{Q}_{n_1}^{c_1} (\mathbf{Q}_{n_1}^{c_1})^*\rangle}\sqrt{\langle (\mathbf{Q}_{n_2}^{c_2})(\mathbf{Q}_{n_2}^{c_2})^*\rangle}} \quad (27)$$

and

$$\cos\left[c_1 n_1 \Psi_{n_1} + c_2 n_2 \Psi_{n_2} - c_3 n_3 \Psi_{n_3}\right] = \frac{\mathrm{Re}\left\{\langle \mathbf{Q}_{n_1}^{c_1} \mathbf{Q}_{n_2}^{c_2} (\mathbf{Q}_{n_3}^{c_3})^*\rangle\right\}}{\sqrt{\langle \mathbf{Q}_{n_1}^{c_1} (\mathbf{Q}_{n_1}^{c_1})^*\rangle\langle (\mathbf{Q}_{n_2}^{c_2})(\mathbf{Q}_{n_2}^{c_2})^*\rangle\langle (\mathbf{Q}_{n_3}^{c_3})(\mathbf{Q}_{n_3}^{c_3})^*\rangle}}, \quad (28)$$

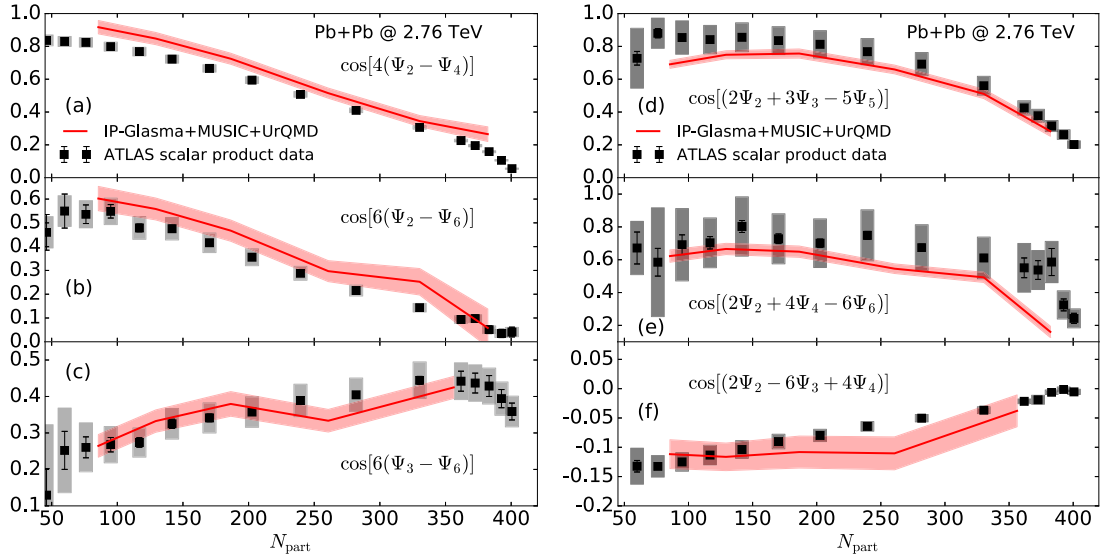

FIG. 13. The charged hadron event-plane correlations are compared with the ATLAS measurements [74] using the scalar-product method in Pb+Pb collisions at 2.76 TeV. The values of N_{part} at different centrality bins are estimated using the MC-Glauber model according to Table I in Ref. [74].

where the particle flow vector $\mathbf{Q}_n$ is defined in Eq. (23). The imaginary part of the correlation function goes to zero after the event average [76]. In the six panels of Fig. 13, our results show fairly good agreement with the experimental measurement as a function of centrality. In panels (c) and (f), the event-plane correlators $\cos[6(\Psi_3-\Psi_6)]$ and $\cos[2\Psi_2-6\Psi_3+4\Psi_4]$ require larger statistics compared to the others. We combined the events in central 0–5% and 5–10% bins to 0–10% to reduce the statistical noise in our results. In Fig. 14, predictions of the flow event-plane correlations at 5.02 TeV are shown. Compared with the results at 2.76 TeV, the correlation strengths are similar at higher collision energies. This reflects that the hydrodynamic response is very similar in the two collision energies.

Figure 15 further show the flow factorization breaking ratios $r_{2,3}$ in Pb+Pb collision at 2.76 TeV compared to the CMS measurements [77]. This r_n ratios reflect the correlations of $v_n(p_T)$ in different p_T bins,

$$r_n\left(p_T^{\rm trig},p_T^{\rm asso}\right) = \frac{\mathrm{Re}\left\{\left\langle \mathbf{Q}_n\left(p_T^{\rm trig}\right)\left(\mathbf{Q}_n\left(p_T^{\rm asso}\right)\right)^*\right\rangle\right\}}{\sqrt{\left\langle \mathbf{Q}_n\left(p_T^{\rm trig}\right)\mathbf{Q}_n^*\left(p_T^{\rm trig}\right)\right\rangle\left\langle \mathbf{Q}_n\left(p_T^{\rm asso}\right)\mathbf{Q}_n^*\left(p_T^{\rm asso}\right)\right\rangle}}. \quad (29)$$

Our hybrid calculations reproduce fairly well the CMS measured $r_{2,3}(p_T^{\rm trig},p_T^{\rm asso})$ in both central and semi-peripheral centrality bins. A sharp drop in the r_3 ratio is found in the theoretical calculation at large values of $p_T^{\rm trig}-p_T^{\rm asso}$. About 75% of the factorization breaking in this p_T bin can be traced

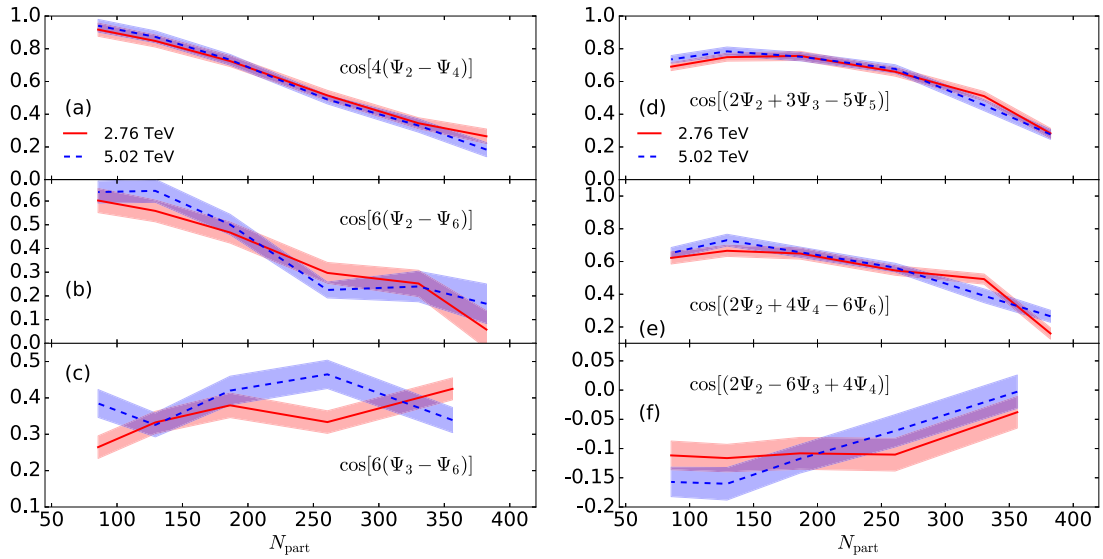

FIG. 14. Predictions of charged hadron event-plane correlations in Pb+Pb collisions at 5.02 TeV.

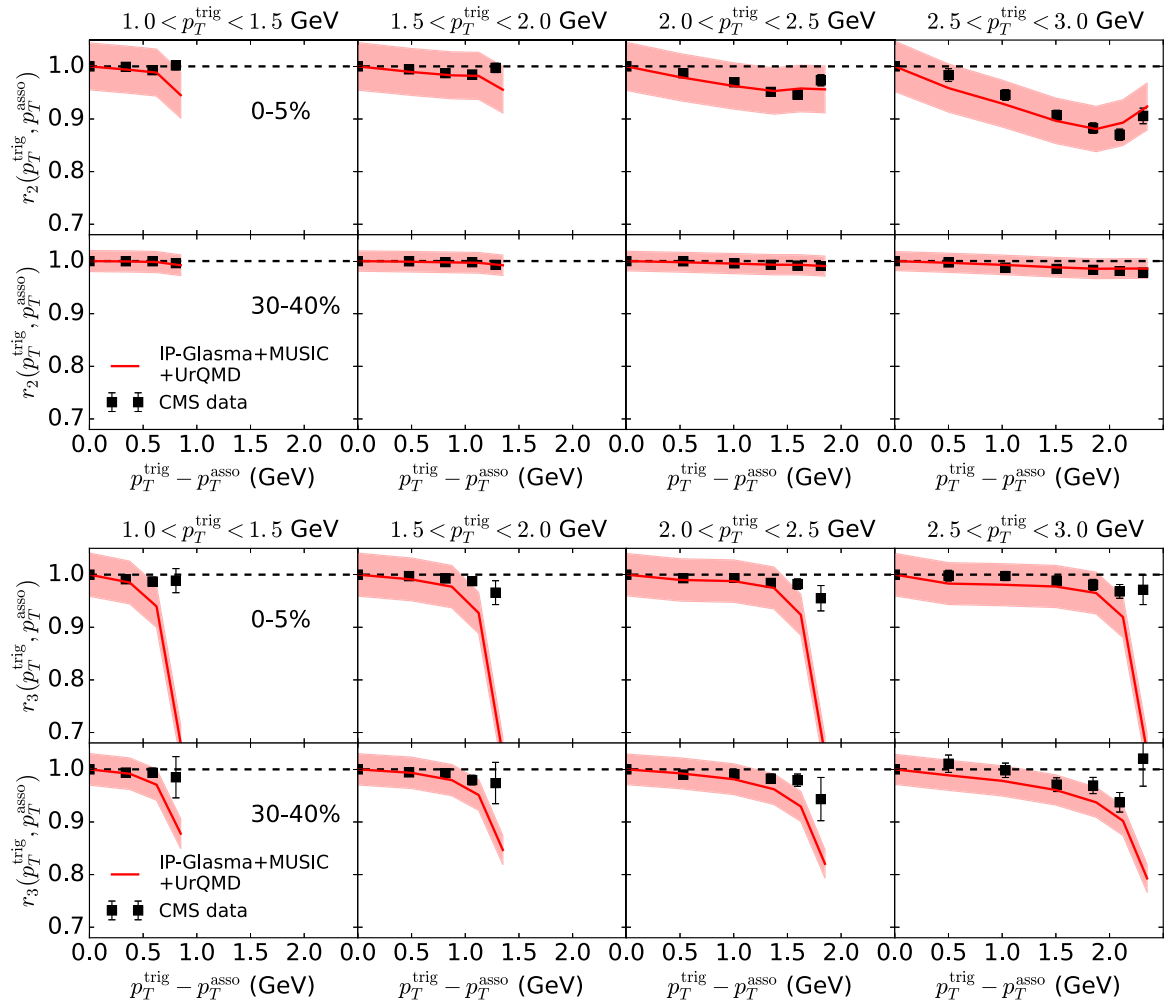

FIG. 15. The charged hadron flow factorization breaking ratio r_n are compared with the CMS measurements [77] in Pb+Pb collisions at 2.76 TeV.

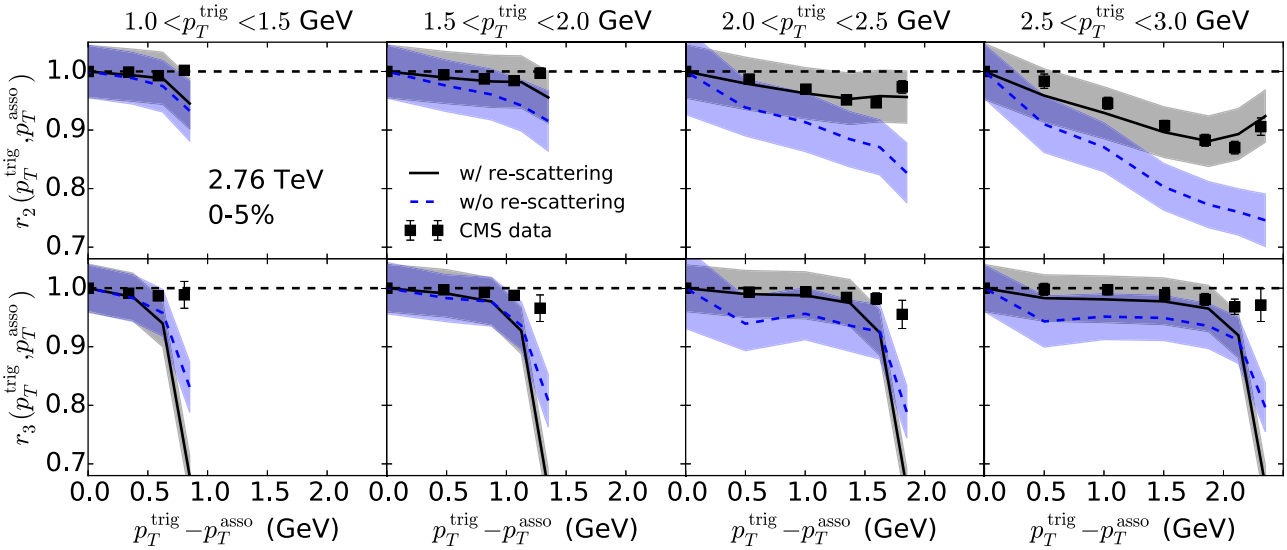

FIG. 16. The effect of hadronic rescatterings on the flow factorization breaking ratios r_2 and r_3.

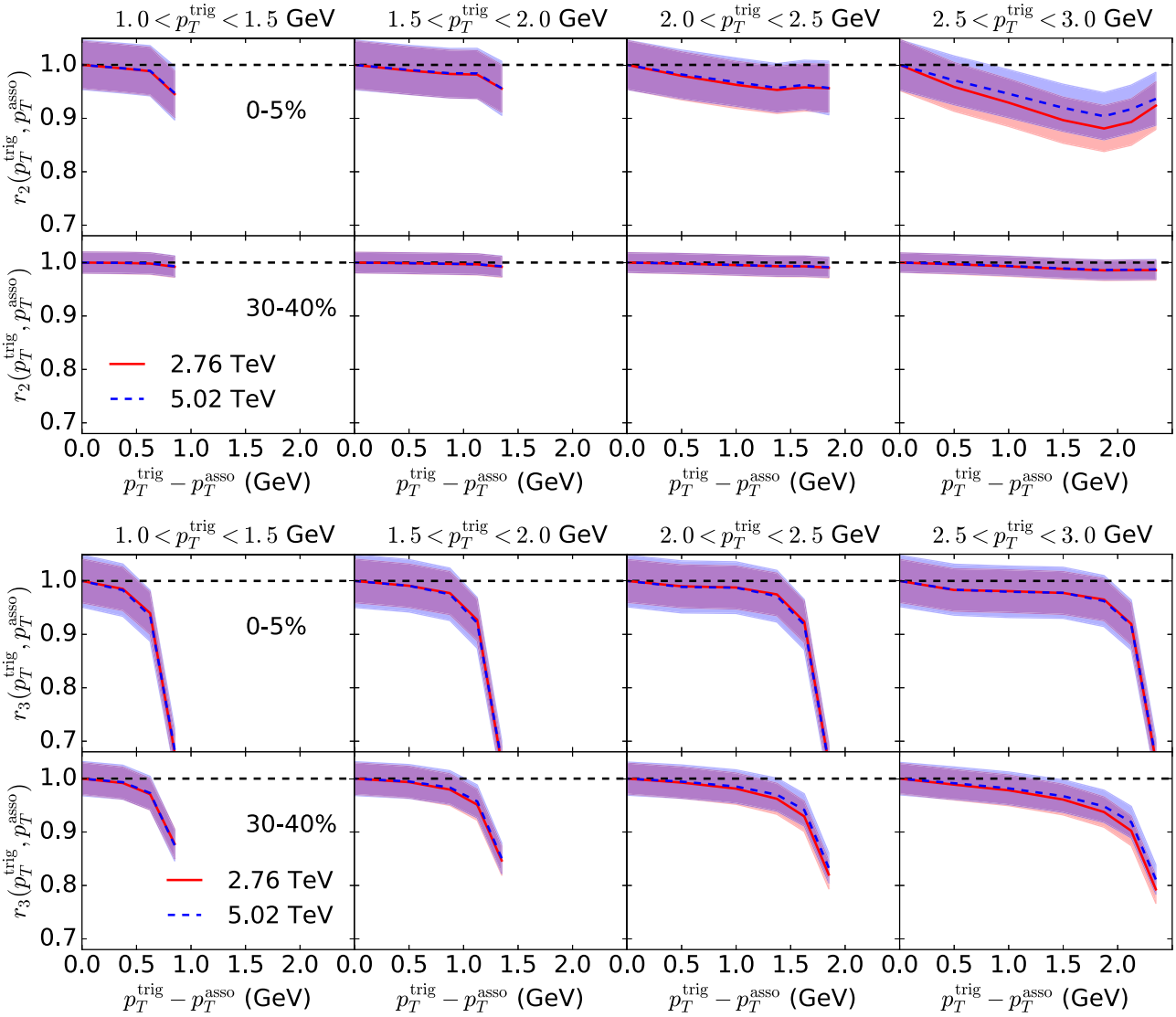

FIG. 17. Predictions of charged hadron flow factorization breaking ratio in Pb+Pb collisions at 5.02 TeV.

back to the flow angle decorrelation between $\Psi_3(p_T^{\rm trig})$ and $\Psi_3(p_T^{\rm asso})$. Figure 16 illustrates the effects of hadronic rescatterings on the flow factorization breaking ratios. For the r_2 ratio, the scattering among hadrons increases the correlations of $v_2(p_T)$ at different p_T bins. The situation becomes a little bit complicated for the r_3 ratio. The additional hadronic scatterings strengthen the correlations for $v_3(p_T)$ among different p_T bins with $p_T > 0.5$ GeV. For $p_T < 0.5$ GeV (the largest value of $p_T^{\rm trig} - p_T^{\rm asso}$), hadronic scatterings randomize the v_3 flow angle. This randomization seems not present for $n = 2$ but is more severe for high order of n. Finally, Fig. 17 predicts the $r_{2,3}$ ratio at the new 5.02 TeV. The magnitude of factorization breaking is about the same at both collision energies.

IV. CONCLUSIONS

In this work, we provided quantitative predictions for hadronic flow observables in Pb+Pb collisions at the new 5.02 TeV collision energy of the LHC. As a starting point of our predictions, we demonstrated that our hybrid framework provided excellent descriptions of a variety of current existing flow measurements in Pb+Pb collisions at 2.76 TeV. The anisotropic flow results of extrapolating to 5.02 TeV showed excellent agreement with the recent ALICE measurements. Such a successful postdiction, together with the fact that the same effective shear viscosity was used at two collision energies, suggest the temperature dependence of $\eta/s(T)$ is rather mild above T_c. Detailed predictions of identified particle observables are provided. Future comparison with experimental data can help us to better understand the dynamical evolution of the collision systems, especially the dynamics in the hadronic phase. Event-by-event distributions of anisotropic flow coefficients and flow correlations among them are studied at the two collision energies of the LHC. The p_T dependence and centrality dependence of these correlation observables remain qualitatively the same at 5.02 TeV compared to those measured at 2.76 TeV. The small quantitative changes can help to test the variation of hydrodynamic response at higher collision energies.

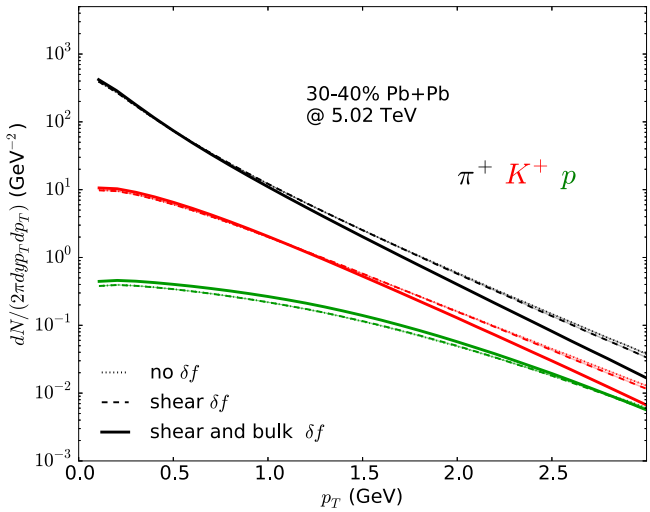

FIG. 18. Identified particle spectra with and without δf corrections from shear and bulk viscosities.

In future work, we will embed the QCD jet showers and minijets contribution into our hydrodynamic medium. The results of this approach can improve the description of particle spectra and flow anisotropy coefficients at intermediate p_T regions, $p_T \gtrsim 2$ GeV. The violation of the mass ordering of multistrange hadrons in the hybrid calculations needs a more detailed study in the hadronic transport model. With the calibrated medium, studies on penetrating observables, such as direct photons and energy loss of QCD jets, will be presented in a forthcoming publication.

ACKNOWLEDGMENTS

This work was supported in part by the Natural Sciences and Engineering Research Council of Canada. Computations were made in part on the supercomputer Guillimin from McGill University, managed by Calcul Québec and Compute Canada. The operation of this supercomputer is funded by the Canada Foundation for Innovation (CFI), NanoQuébec, RMGA, and the Fonds de recherche du Québec - Nature et technologies (FRQ-NT). Finally, we would like to thank Björn Schenke for insightful discussions and for providing his IP-Glasma code for detailed numerical cross checking.

APPENDIX: THE EFFECTS OF OUT-OF-EQUILIBRIUM CORRECTION δf ON FLOW OBSERVABLES

In this work, the form of out-of-equilibrium correction δf in the Cooper-Frye freeze-out is chosen as that derived from the Boltzmann equation assuming a relaxation time approximation. The exact forms of δf for shear and bulk viscosities are still unknown. Moreover, because the δf correction increases with p_T, higher order corrections are more important and cannot be neglected at high p_T. So δf corrections introduce theoretical uncertainties in our results. In this appendix, we would like to study the sensitivity of the δf corrections to hadronic flow observables.

Figure 18 shows the effect of shear and bulk δf on identified particle p_T spectra. The shear δf only modifies the particle spectra slightly. This is because the specific shear viscosity $\eta/s = 0.095$ is relatively small in our calculation. The size of shear stress tensor $\pi^{\mu\nu}$ is small at the freeze-out. Meanwhile, the out-of-equilibrium correction from bulk viscosity plays an important role. The bulk δf steepens the particle spectra. The expression for bulk δf, given in Eq. (22), has two terms: a mass dependent term that increases particle yield at low energy and a negative term that increases linearly with energy. The transition from positive to negative correction happens at momentum $p = m\sqrt{3c_s^2/(1-3c_s^2)}$. The pion and kaon spectra are suppressed for $p_T > 1.5$ GeV. For heavier protons, this transition happens at ~2.5 GeV. The low p_T proton spectra are enhanced, which leads to an increase in the particle yield.

The δf effects on particle p_T-differential $v_{2,3}(p_T)$ are studied in Fig. 19. The shear δf suppresses $v_n(p_T)$ while the bulk δf increases it. Because the bulk δf correction is isotropic, the increase of $v_n(p_T)$ is because the particle spectra are strongly suppressed by the δf^{bulk}. The magnitude of bulk δf correction is larger than the shear correction. So the identified particle $v_n(p_T)$ increases with δf corrections.

In Fig. 20, we study the effects of shear and bulk δf on the flow factorization breaking ratios r_2 and r_3. Both shear and bulk δf have negligible effects on the r_2 ratio in all p_T bins.

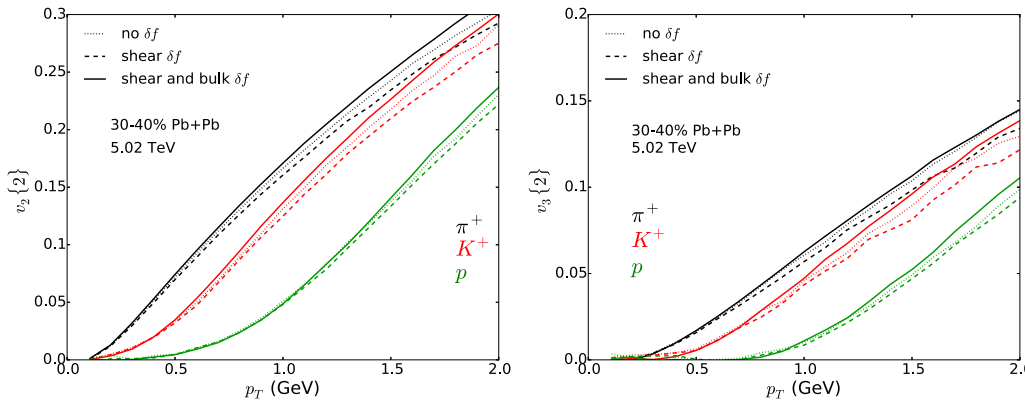

FIG. 19. Identified particle p_T-differential $v_2(p_T)$ and $v_3(p_T)$ with and without the shear and bulk δf corrections.

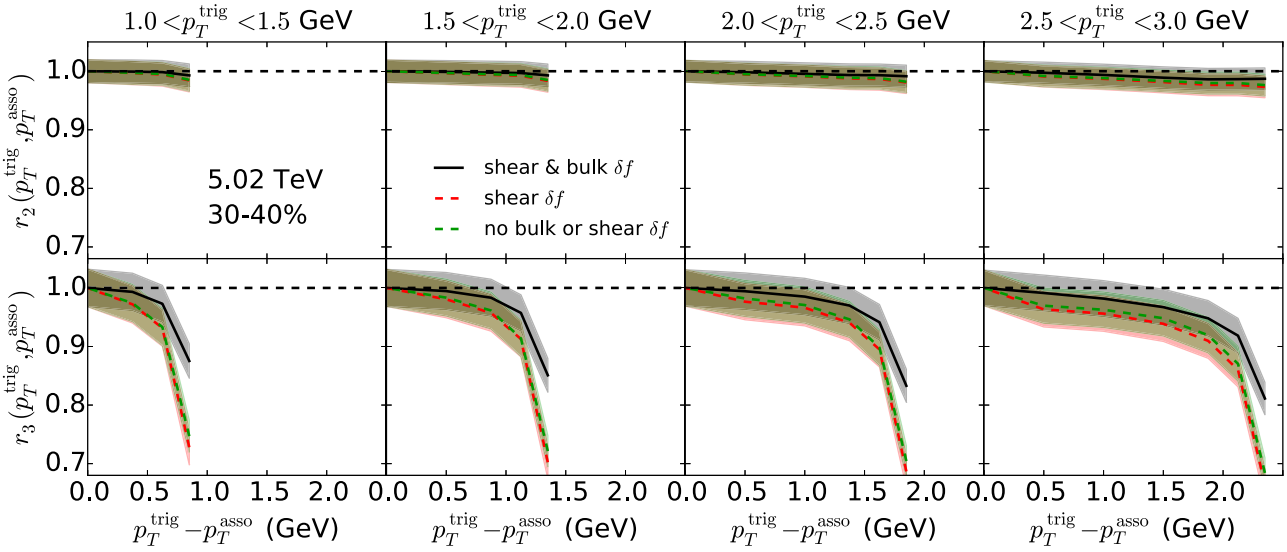

FIG. 20. The effect of shear and bulk δf on the flow factorization breaking ratios r_2 and r_3.

The bulk viscous δf suppresses the r_3 ratio at large difference between $p_T^{\rm trig}$ and $p_T^{\rm asso}$. This means that the triangular flow correlation between small and large p_T bins is reduced by the bulk viscous δf.

[1] C. Gale, S. Jeon, and B. Schenke, Hydrodynamic modeling of heavy-ion collisions, Int. J. Mod. Phys. A **28**, 1340011 (2013).

[2] U. Heinz and R. Snellings, Collective flow and viscosity in relativistic heavy-ion collisions, Annu. Rev. Nucl. Part. Sci. **63**, 123 (2013).

[3] J. Adam *et al.* (ALICE Collaboration), Anisotropic Flow of Charged Particles in Pb−Pb Collisions at $\sqrt{s_{\rm NN}} = 5.02$ TeV, Phys. Rev. Lett. **116**, 132302 (2016).

[4] S. Ryu, J. F. Paquet, C. Shen, G. S. Denicol, B. Schenke, S. Jeon, and C. Gale, Importance of the Bulk Viscosity of QCD in Ultrarelativistic Heavy-Ion Collisions, Phys. Rev. Lett. **115**, 132301 (2015).

[5] S. A. Bass *et al.*, Microscopic models for ultrarelativistic heavy ion collisions, Prog. Part. Nucl. Phys. **41**, 255 (1998).

[6] M. Bleicher *et al.*, Relativistic hadron hadron collisions in the ultrarelativistic quantum molecular dynamics model, J. Phys. G **25**, 1859 (1999).

[7] H. Niemi, K. J. Eskola, R. Paatelainen, and K. Tuominen, Predictions for 5.023 TeV Pb + Pb collisions at the CERN Large Hadron Collider, Phys. Rev. C **93**, 014912 (2016).

[8] J. Noronha-Hostler, M. Luzum, and J.-Y. Ollitrault, Hydrodynamic predictions for 5.02 TeV Pb−Pb collisions, Phys. Rev. C **93**, 034912 (2016).

[9] G.-L. Ma and Z.-W. Lin, Predictions for $\sqrt{s_{NN}} = 5.02$ TeV Pb+Pb collisions from a multiphase transport model, Phys. Rev. C **93**, 054911 (2016).

[10] S. Ryu, J.-F. Paquet, C. Shen, G. Denicol, B. Schenke, S. Jeon, and C. Gale, Effects of bulk viscosity and hadronic rescattering in heavy ion collisions at RHIC and LHC, arXiv:1704.04216 [nucl-th].

[11] J. E. Bernhard, J. S. Moreland, S. A. Bass, J. Liu, and U. Heinz, Applying Bayesian parameter estimation to relativistic heavy-ion collisions: Simultaneous characterization of the initial state and quark-gluon plasma medium, Phys. Rev. C **94**, 024907 (2016).

[12] H. Niemi, K. J. Eskola, and R. Paatelainen, Event-by-event fluctuations in a perturbative QCD + saturation + hydrodynamics model: Determining QCD matter shear viscosity in ultrarelativistic heavy-ion collisions, Phys. Rev. C **93**, 024907 (2016).

[13] B. Schenke, P. Tribedy, and R. Venugopalan, Event-by-event gluon multiplicity, energy density, and eccentricities in ultrarelativistic heavy-ion collisions, Phys. Rev. C **86**, 034908 (2012).

[14] B. Schenke, P. Tribedy, and R. Venugopalan, Fluctuating Glasma Initial Conditions and Flow in Heavy Ion Collisions, Phys. Rev. Lett. **108**, 252301 (2012).

[15] H. Kowalski and D. Teaney, An Impact parameter dipole saturation model, Phys. Rev. D **68**, 114005 (2003).

[16] A. Krasnitz and R. Venugopalan, Non-perturbative computation of gluon mini-jet production in nuclear collisions at very high energies, Nucl. Phys. B **557**, 237 (1999).

[17] A. Krasnitz and R. Venugopalan, Initial Energy Density of Gluons Produced in Very-High-Energy Nuclear Collisions, Phys. Rev. Lett. **84**, 4309 (2000).

[18] A. Krasnitz, Y. Nara, and R. Venugopalan, Coherent Gluon Production in Very-High-Energy Heavy-Ion Collisions, Phys. Rev. Lett. **87**, 192302 (2001).

[19] A. Krasnitz and R. Venugopalan, Initial Gluon Multiplicity in Heavy-Ion Collisions, Phys. Rev. Lett. **86**, 1717 (2001).

[20] K. Fukushima and F. Gelis, The evolving Glasma, Nucl. Phys. A **874**, 108 (2012).

[21] H. De Vries, C. W. De Jager, and C. De Vries, Nuclear charge and magnetization density distribution parameters from elastic electron scattering, At. Data Nucl. Data Tables **36**, 495 (1987).

[22] M. Alvioli, H. J. Drescher, and M. Strikman, A Monte Carlo generator of nucleon configurations in complex nuclei including nucleon-nucleon correlations, Phys. Lett. B **680**, 225 (2009).

[23] C. Shen, Z. Qiu, and U. Heinz, Shape and flow fluctuations in ultracentral Pb + Pb collisions at the energies available at the CERN Large Hadron Collider, Phys. Rev. C **92**, 014901 (2015).

[24] A. H. Rezaeian, M. Siddikov, M. Van de Klundert, and R. Venugopalan, Analysis of combined HERA data in the impact-parameter dependent saturation model, Phys. Rev. D **87**, 034002 (2013).

[25] Y. L. Dokshitzer, Calculation of the structure functions for deep inelastic scattering and e^+-e^- annihilation by perturbation theory in quantum chromodynamics, Sov. Phys. JETP **46**, 641 (1977).

[26] G. Altarelli and G. Parisi, Asymptotic freedom in parton language, Nucl. Phys. B **126**, 298 (1977).

[27] V. N. Gribov and L. N. Lipatov, Deep inelastic e-p scattering in perturbation theory, Sov. J. Nucl. Phys. **15**, 438 (1972).

[28] F. Gelis, Software (DGLAP equation), http://ipht.cea.fr/Pisp/francois.gelis/Soft/DGLAP/index.php, accessed July 5, 2016.

[29] T. Lappi, Wilson line correlator in the MV model: Relating the glasma to deep inelastic scattering, Eur. Phys. J. C **55**, 285 (2008).

[30] A. Kovner, L. McLerran, and H. Weigert, Gluon production from non-Abelian Weizsäcker-Williams fields in nucleus-nucleus collisions, Phys. Rev. D **52**, 6231 (1995).

[31] A. Kovner, L. McLerran, and H. Weigert, Gluon production at high transverse momentum in the Mclerran-Venugopalan model of nuclear structure functions, Phys. Rev. D **52**, 3809 (1995).

[32] T. Lappi, Production of gluons in the classical field model for heavy ion collisions, Phys. Rev. C **67**, 054903 (2003).

[33] F. G. Gardim, F. Grassi, Y. Hama, M. Luzum, and J.-Y. Ollitrault, Directed flow at mid-rapidity in event-by-event hydrodynamics, Phys. Rev. C **83**, 064901 (2011).

[34] G. Vujanovic, J.-F. Paquet, G. S. Denicol, M. Luzum, S. Jeon, and C. Gale, Electromagnetic radiation as a probe of the initial state and of viscous dynamics in relativistic nuclear collisions, Phys. Rev. C **94**, 014904 (2016).

[35] B. Abelev *et al.* (ALICE Collaboration), Centrality determination of Pb−Pb collisions at $\sqrt{s_{NN}} = 2.76$ TeV with ALICE, Phys. Rev. C **88**, 044909 (2013).

[36] V. Khachatryan *et al.* (CMS Collaboration), Evidence for collectivity in pp collisions at the LHC, Phys. Lett. B **765**, 193 (2017).

[37] B. Schenke, S. Jeon, and C. Gale, Elliptic and Triangular Flow in Event-by-Event (3+1)D Viscous Hydrodynamics, Phys. Rev. Lett. **106**, 042301 (2011).

[38] P. Huovinen and P. Petreczky, QCD equation of state and hadron resonance gas, Nucl. Phys. A **837**, 26 (2010).

[39] G. S. Denicol, S. Jeon, and C. Gale, Transport coefficients of bulk viscous pressure in the 14-moment approximation, Phys. Rev. C **90**, 024912 (2014).

[40] C. Shen, Z. Qiu, H. Song, J. Bernhard, S. Bass, and U. Heinz, The iEBE-VISHNU code package for relativistic heavy-ion collisions, Comput. Phys. Commun. **199**, 61 (2016).

[41] M. Floris, Hadron yields and the phase diagram of strongly interacting matter, Nucl. Phys. A **931**, 103 (2014).

[42] J. Steinheimer, J. Aichelin, and M. Bleicher, Nonthermal p/π Ratio at LHC as a Consequence of Hadronic Final State Interactions, Phys. Rev. Lett. **110**, 042501 (2013).

[43] F. Karsch, D. Kharzeev, and K. Tuchin, Universal properties of bulk viscosity near the QCD phase transition, Phys. Lett. B **663**, 217 (2008).

[44] J. Noronha-Hostler, J. Noronha, and C. Greiner, Transport Coefficients of Hadronic Matter Near T_c, Phys. Rev. Lett. **103**, 172302 (2009).

[45] A. Bazavov, T. Bhattacharya, C. DeTar, H.T. Ding, S. Gottlieb, R. Gupta, P. Hegde, U.M. Heller, F. Karsch, E. Laermann, L. Levkova, S. Mukherjee, P. Petreczky, C. Schmidt, C. Schroeder, R.A. Soltz, W. Soeldner, R. Sugar, M. Wagner, and P. Vranas (HotQCD Collaboration), Equation of state in (2+1)-flavor QCD, Phys. Rev. D **90**, 094503 (2014).

[46] G. Aad *et al.* (ATLAS Collaboration), Measurement of the azimuthal anisotropy for charged particle production in $\sqrt{s_{NN}} = 2.76$ TeV lead-lead collisions with the ATLAS detector, Phys. Rev. C **86**, 014907 (2012).

[47] G. Aad *et al.* (ATLAS Collaboration), Measurement of the distributions of event-by-event flow harmonics in lead-lead collisions at $\sqrt{s_{NN}} = 2.76$ TeV with the ATLAS detector at the LHC, J. High Energy Phys. 11 (2013) 183.

[48] K. Aamodt *et al.* (ALICE Collaboration), Centrality Dependence of the Charged-Particle Multiplicity Density at Mid-Rapidity in Pb−Pb Collisions at $\sqrt{s_{NN}} = 2.76$ TeV, Phys. Rev. Lett. **106**, 032301 (2011).

[49] J. Adam *et al.* (ALICE Collaboration), Centrality Dependence of the Charged-Particle Multiplicity Density at Midrapidity in Pb−Pb Collisions at $\sqrt{s_{\rm NN}} = 5.02$ TeV, Phys. Rev. Lett. **116**, 222302 (2016).

[50] K. Aamodt *et al.* (ALICE Collaboration), Higher Harmonic Anisotropic Flow Measurements of Charged Particles in Pb−Pb Collisions at $\sqrt{s_{NN}} = 2.76$ TeV, Phys. Rev. Lett. **107**, 032301 (2011).

[51] M. Luzum and J.-Y. Ollitrault, Eliminating experimental bias in anisotropic-flow measurements of high-energy nuclear collisions, Phys. Rev. C **87**, 044907 (2013).

[52] R. P. G. Andrade, J. Noronha, and G. S. Denicol, Jet quenching effects on the direct, elliptic, and triangular flow at energies available at the BNL Relativistic Heavy Ion Collider, Phys. Rev. C **90**, 024914 (2014).

[53] M. Schulc and B. Tomášik, Anisotropic flow of the fireball fed by hard partons, Phys. Rev. C **90**, 064910 (2014).

[54] J. Crkovska, J. Bielcik, L. Bravina, B. H. Johansson, E. Zabrodin, G. Eyyubova, V. L. Korotkikh, I. P. Lokhtin, L. V. Malinina, S. V. Petrushanko, and A. M. Snigirev, Influence of jets and decays of resonances on the triangular flow in ultrarelativistic heavy-ion collisions, Phys. Rev. C **95**, 014910 (2017).

[55] S. Ryu, S. McDonald, C. Shen, S. Jeon, and C. Gale (unpublished).

[56] C. Gale, S. Jeon, B. Schenke, P. Tribedy, and R. Venugopalan, Event-by-Event Anisotropic Flow in Heavy-Ion Collisions from Combined Yang-Mills and Viscous Fluid Dynamics, Phys. Rev. Lett. **110**, 012302 (2013).

[57] B. Abelev *et al.* (ALICE Collaboration), Centrality dependence of π, K, p production in Pb−Pb collisions at $\sqrt{s_{NN}} = 2.76$ TeV, Phys. Rev. C **88**, 044910 (2013).

[58] R. Bellwied, S. Borsanyi, Z. Fodor, S. D. Katz, and C. Ratti, Is There a Flavor Hierarchy in the Deconfinement Transition of QCD? Phys. Rev. Lett. **111**, 202302 (2013).

[59] A. Bazavov, H.T. Ding, P. Hegde, O. Kaczmarek, F. Karsch, E. Laermann, Y. Maezawa, S. Mukherjee, H. Ohno, P. Petreczky, C. Schmidt, S. Sharma, W. Soeldner, and M. Wagner, Additional Strange Hadrons from QCD Thermodynamics and Strangeness Freezeout in Heavy Ion Collisions, Phys. Rev. Lett. **113**, 072001 (2014).

[60] B. B. Abelev *et al.* (ALICE Collaboration), Multi-strange baryon production at mid-rapidity in Pb−Pb collisions at $\sqrt{s_{NN}} = 2.76$ TeV, Phys. Lett. B **728**, 216 (2014); **734**, 409(E) (2014).

[61] B. B. Abelev *et al.* (ALICE Collaboration), K^0_S and Λ Production in Pb−Pb Collisions at $\sqrt{s_{NN}} = 2.76$ TeV, Phys. Rev. Lett. **111**, 222301 (2013).

[62] B. B. Abelev *et al.* (ALICE Collaboration), $K^*(892)^0$ and $\phi(1020)$ production in Pb−Pb collisions at $\sqrt{sNN} = 2.76$ TeV, Phys. Rev. C **91**, 024609 (2015).

[63] J. Beringer *et al.* (Particle Data Group), Review of particle physics (RPP), Phys. Rev. D **86**, 010001 (2012).

[64] B. B. Abelev *et al.* (ALICE Collaboration), Elliptic flow of identified hadrons in Pb−Pb collisions at $\sqrt{s_{\rm NN}} = 2.76$ TeV, J. High Energy Phys. 06 (2015) 190.

[65] C. Shen and U. Heinz, Collision energy dependence of viscous hydrodynamic flow in relativistic heavy-ion collisions, Phys. Rev. C **85**, 054902 (2012); **86**, 049903(E) (2012).

[66] C. Shen, U. Heinz, P. Huovinen, and H. Song, Radial and elliptic flow in Pb+Pb collisions at the Large Hadron Collider from viscous hydrodynamics, Phys. Rev. C **84**, 044903 (2011).

[67] J. Adam *et al.* (ALICE Collaboration), Higher harmonic flow coefficients of identified hadrons in Pb−Pb collisions at $\sqrt{s_{\rm NN}} = 2.76$ TeV, J. High Energy Phys. 09 (2016) 164.

[68] H.-J. Xu, Z. Li, and H. Song, High-order flow harmonics of identified hadrons in 2.76*A* TeV Pb+Pb collisions, Phys. Rev. C **93**, 064905 (2016).

[69] X. Zhu, F. Meng, H. Song, and Y.-X. Liu, Hybrid model approach for strange and multistrange hadrons in 2.76*A* TeV Pb+Pb collisions, Phys. Rev. C **91**, 034904 (2015).

[70] S. Takeuchi, K. Murase, T. Hirano, P. Huovinen, and Y. Nara, Effects of hadronic rescattering on multistrange hadrons in high-energy nuclear collisions, Phys. Rev. C **92**, 044907 (2015).

[71] S. Takeuchi, K. Murase, T. Hirano, P. Huovinen, and Y. Nara, Violation of mass ordering for multi-strange hadrons at RHIC and LHC, Proceedings of the 25th International Conference on Ultra-Relativistic Nucleus-Nucleus Collisions (Quark Matter 2015): Kobe, Japan, September 27–October 3, 2015 [Nucl. Phys. A **956**, 457 (2016)].

[72] X. Zhu, Spectra and elliptic flow of (multi-)strange hadrons at RHIC and LHC within viscous hydrodynamics + hadron cascade hybrid model, Adv. High Energy Phys. **2016**, 4236492 (2016).

[73] J. Noronha-Hostler, L. Yan, F. G. Gardim, and J.-Y. Ollitrault, Linear and cubic response to the initial eccentricity in heavy-ion collisions, Phys. Rev. C **93**, 014909 (2016).

[74] G. Aad *et al.* (ATLAS Collaboration), Measurement of event-plane correlations in $\sqrt{s_{NN}} = 2.76$ TeV lead-lead collisions with the ATLAS detector, Phys. Rev. C **90**, 024905 (2014).

[75] J. Jia, Event-shape fluctuations and flow correlations in ultra-relativistic heavy-ion collisions, J. Phys. G **41**, 124003 (2014).

[76] U. Heinz, Z. Qiu, and C. Shen, Fluctuating flow angles and anisotropic flow measurements, Phys. Rev. C **87**, 034913 (2013).

[77] V. Khachatryan *et al.* (CMS Collaboration), Evidence for transverse momentum and pseudorapidity dependent event plane fluctuations in Pb−Pb and p−Pb collisions, Phys. Rev. C **92**, 034911 (2015).